metals

MDPI

Review

Conceptual Analysis on Severe Plastic Deformation Processes of Shape Memory Alloys: Mechanical Properties and Microstructure Characterization

Mahmoud Ebrahimi [1,*], Shokouh Attarilar [2], Ceren Gode [3], Sumanth Ratna Kandavalli [4], Mahmoud Shamsborhan [5,6] and Qudong Wang [7,*]

1 Department of Mechanical Engineering, Faculty of Engineering, University of Maragheh, Maragheh 83111-55181, Iran
2 Department of Materials Engineering, Faculty of Engineering, University of Maragheh, Maragheh 83111-55181, Iran
3 Department of Mechanical and Metal Technologies, Denizli Vocational School of Technical Sciences, Pamukkale University, Denizli 20160, Turkey
4 Department of Mechanical Engineering, Tandon School of Engineering, New York University, Brooklyn, 6 MetroTech Center, New York, NY 11201, USA
5 Department of Mechanical Engineering, College of Engineering, University of Zakho, Zakho 42002, Iraq
6 Department of Mechanical Engineering, Mahabad Branch, Islamic Azad University, Mahabad 14778-93855, Iran
7 National Engineering Research Center of Light Alloy Net Forming and State Key Laboratory of Metal Matrix Composites, School of Materials Science and Technology, Shanghai Jiao Tong University, Shanghai 200240, China
* Correspondence: ebrahimi@maragheh.ac.ir (M.E.); wangqudong@sjtu.edu.cn (Q.W.)

Abstract: Shape memory alloys (SMAs) are types of materials that can restore their original shape upon severe or quasi-plastic deformation, being exposed to specific external stimuli, including heating, electric current, magnetic field, etc. They are a category of functional materials that provides superelasticity as a significant material property. The roots of this unintentional discovery were in the 20th century, and later it attracted the attention of various industries, including aerospace, medical, mechanical, manufacturing industries, etc. Later developments mainly focused on improving the properties of these materials. One of the ways in which this is achieved is the application of intensive plastic strains on SMAs through severe plastic deformation (SPD) methods, leading to extreme grain refinement. Superelasticity is a key characteristic of SMAs and is known as the capacity of a polycrystalline material to display extremely high elongations before failure, in a typically isotropic way, with an approximate strain rate of 0.5. Utilization of SPD techniques can also affect and lead to superior superelasticity responses in SMAs. Several SPD methodologies have been introduced over the decades, to produce ultrafine-grained and even nanostructured materials, including constrained groove pressing, equal-channel angular pressing, high-speed high-pressure torsion, accumulative roll bonding, etc. This paper aims to present a clear view of the mechanical properties and microstructure evolution of shape memory alloys after processing by some SPD methods, and to show that SPD methods can be a great option for developing SMAs and expanding their industrial and technological applications.

Keywords: severe plastic deformation; shape memory alloys; superelasticity; mechanical properties; microstructure evolution

Citation: Ebrahimi, M.; Attarilar, S.; Gode, C.; Kandavalli, S.R.; Shamsborhan, M.; Wang, Q. Conceptual Analysis on Severe Plastic Deformation Processes of Shape Memory Alloys: Mechanical Properties and Microstructure Characterization. *Metals* **2023**, *13*, 447. https://doi.org/10.3390/met13030447

Academic Editors: Nong Gao and Xiaoguang Qiao

Received: 28 December 2022
Revised: 24 January 2023
Accepted: 16 February 2023
Published: 21 February 2023

1. Introduction

Severe plastic deformation (SPD) is a type of thermomechanical material processing technology to obtain metals and alloys with extraordinary properties [1–3]. The application of intensive plastic strains is the main characteristic that distinguishes SPD techniques from the widely-known conventional plastic deformation processes, such as forging, rolling, extrusion, etc. [4]. These techniques were designed to apply high strain magnitudes, with

high rates, between the continuum slip lines to attain considerable plastic deformation. This is an optimal procedure to modify the microstructure of metallic materials through grain refinement, leading to exceptional mechanical properties. Therefore, SPD has gained popularity in scientific society over the past three decades due to its advantages in producing ultrafine-grained (UFG) and even nanostructured (NS) bulk materials, with impressive physical and mechanical properties. Based on this, a variety of SPD methods have been proposed, introduced, and investigated, among which are, equal channel angular pressing [5,6], equal channel forward extrusion [7], cyclic extrusion compression [8], high-pressure torsion [3], accumulative roll bonding [9], constrained groove pressing [10], multi-directional forging [11], friction stir processing [12], planar twist channel angular extrusion [13], and planar twist extrusion [14].

Among various materials, shape memory alloys (SMAs) are unique materials used in different industrial and medical applications [15–17]. They have a wide range of outstanding properties, especially an extraordinary energy dissipation capacity compared to traditional metallic materials. The history of SMAs dates back to the early 19th century when the first SMAs were discovered by Arne Olander in 1932 [18], they were later popularized in 1962 by Wang and Buehler [19]. The shape memory feature provides new enticing progress into materials research, opening previously unknown frontiers and enabling access to novel functionalities. As a result, researchers in the field of mechanics, intending to produce materials with surprising properties to meet stringent requirements, have developed a renewed interest in shape memory materials. The shape memory effect makes SMA materials very attractive for a wide range of engineering and medical applications [20–26]. The shape memory effect (SME) is caused by martensitic transformation (M_T) [27,28]. Also, the shape memory effect and superelasticity (SE) are responsible for the rapid response of processes, reversibility, and repeatability [29]. The main difference between the SME and SE behaviors is demonstrated in Figure 1, by the tensile stress-strain curve [30]. It is known that an increase in the heat-treatment temperature can improve the shape recovery rate due to phase transformations. In this regard, the amount of provided martensite, the number of dislocations and vacancies in the alloy, and the rate of martensite to austenite transformation can be determined according to the SME degree [31,32]. SMAs also have a high elastic elongation, of about 8%, a unique property known as superelasticity. Meanwhile, by increasing the alloy temperature above a particular range, SMAs can restore their original shape from up to 15% elongation, which is known as pseudoelasticity [16].

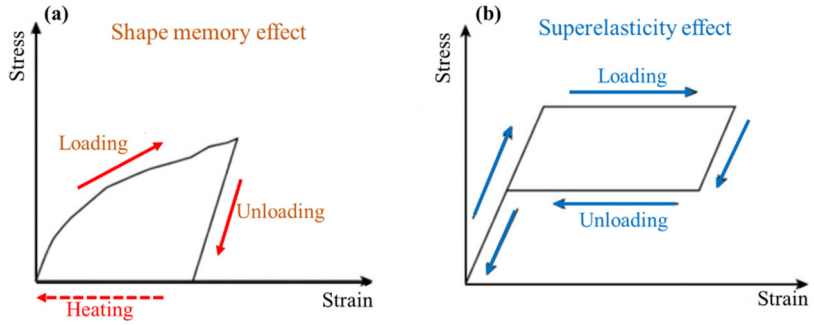

Figure 1. Representation of the difference between (**a**) shape memory effect and (**b**) superelasticity in the tensile stress-strain curve.

Elaborating further on SMAs, it should be noted that NiTi, or Nitinol, alloys are regarded as the most well-known SMAs, in which the amount of nickel can vary between 40 and 60% [33,34]. These NiTi alloys can withstand a relatively high actuation stress, with extensive application in lightweight actuators. Also, due to the high electrical resistance of NiTi alloys and their low price compared to other SMAs, they have found many applications, such as transmission valves and shape-morphing structures in aircraft wings [33,35]. Moreover, NiTi alloys are among the most commonly used SMAs due to their properties, such as significant recoverable deformation, exceptional SME and SE

behavior in the temperature range of −200 to 200 °C, acceptable damping capability, and outstanding mechanical properties.

Although the application of Nitinol has many advantages, if its strength and toughness can be increased to some extent, it can be utilized in higher-strength structures. In this regard, some scientists have used procedures such as severe plastic deformation techniques to further improve its properties. It has been found that many mechanical and physical properties, including yield strength, ultimate tensile strength, hardness, fatigue endurance, corrosion, etc., are enhanced significantly through SPD methods. In addition, electrical resistance, thermal conductivity, friction and wear behavior, and damping are several examples [25]. It has been determined that the favorable magnetic property is achieved by decreasing the coercivity and Curie temperatures, as a result of grain size reduction through the application of the SPD process. The disappearance of M_T could be explained by sample nanostructuring and probable amorphization at the applied maximum deformation degree [26].

The stress-strain curve of nanocrystalline/amorphous NiTi is unusually pseudoelastic, without a stress plateau and hysteresis. Determining the effect of high-density lattice defects and nanoscale grain size in martensitic transformation is prominent in terms of the phase change mechanism [28]. At room temperature, SPD can cause amorphization in a NiTi SMA sample. Just as when amorphous NiTi SMA is aged at 600 °C for 2 h, it crystallizes. Consequently, SPD and subsequent aging contribute to raising the martensite transition temperature. SPD methods also play a crucial role in preventing the R-phase formation and Ni4Ti3 precipitates in NiTi SMA [29]. In particular, the shape memory effect and superelasticity of NiTi SMA make it very attractive. Through the transformation of NiTi SMA, two distinct phases can exist, including B_2 austenite and $B_{19'}$ martensite. As a result, NiTi SMA undergoes a phase change from B_2 austenite to $B_{19'}$ martensite during cooling, and from $B_{19'}$ martensite to B_2 austenite during heating. As soon as a certain deformation occurs in the martensitic phase, the shape memory effect of NiTi SMA (according to its capacity) can restore its previous shape when exposed to temperatures just above the austenite finish temperature (A_f). The stress-induced martensite transition during loading, as well as the spontaneous reversion of the transformation under unloading, is related to the superelasticity property of NiTi SMA, which is defined as a nonlinear recoverable deformation behavior at temperatures above the A_f [30]. Therefore, there is a significant difference between conventional (traditional) alloys and shape memory alloys after applying the SPD technique. In this regard, the grain size reduction is attributed to the hard particles generated as a result of grain refining additives that suppress grain growth during casting, and subsequent beta solution treatment. In addition to mechanical properties, SPD can change other characteristics of SMAs, such as magnetization. It is known that lattice transformation and magnetic phase transition are related to each other in magnetic shape memory alloys [36]. Also, the content of some alloying elements such as Fe, Ni, Co, Cu, Cr, etc., can affect the magnetic properties of shape memory alloys [37–42]. Meanwhile, magnetic-field-induced structural transformation can lead to the generation of staircase-like magnetization in Fe–Mn–Ga shape memory alloys [43].

Besides Nitinol, one of the high-temperature SMAs with the most potential is a ZrCu-based alloy, presenting a high martensitic transformation temperature with a low price and favorable casting fluidity [44]. Compared to Ti alloys, Zr alloys have higher ductility and shape memory strain. Also, when compared to the corresponding base alloys and other Cu-based shape memory alloys, grain refinement increases the shape memory strain by 8%. Certainly, SMAs have a higher hardness with intensive grain refinement [31]. Furthermore, copper-based SMAs are highly interesting due to their mechanical properties associated with martensitic transformation (M_T), such as SME and the superelasticity effect (SE), which contributes to damping capability and high fatigue resistance [45–47]. M_T is a first-order diffusionless phase transition induced by stress in the Cu–Al–Be SMA, where a high-temperature face-centered cubic (FCC) structure transforms it into a low-temperature orthorhombic unit cell [48]. Other special classes of SMAs include Heusler alloys that are able to undergo a martensitic transformation, such as Ni–Fe–Ga [49,50],

Co–Ni–Ga [51], and Ni–Mn–(Ga, Al, In, Sn) [52]. The main structural characteristic of Heusler alloys is their ordered structure, with an FCC superlattice and a BCC unit cell [53,54]. The other group is iron-based SMAs, for instance microstructural studies on the Fe–28Mn–6Si–5Cr alloy indicated the direct effect of grain refinement in the very fast transformation (less than 10 s) of the coarse dendritic structure. Also, the application of severe plastic deformation on Fe–Mn–Si SMA through the HPT process led to grain sizes in the range of 50 to 120 nm. Moreover, the formation of ε_{HCP} martensite has been demonstrated during high-speed HPT processing [55]. There are many varieties of SMAs that are processed through SPD techniques; Table 1 tries to summarize the SPD-processed SMAs along with their applications and main experimental features. The aim of this research is to investigate the different SPD methods and their effects on the different properties of SMAs. It should be noted that we did not assume any technique to be superior to the other, and our criteria was to discuss all the research that was in line with the research goal. It is obvious that due to the limitations in the literature, some techniques have not been investigated at all, and for this reason, they have not been included in our research.

Table 1. Types of shape memory alloys, the applied severe plastic deformation methods, and their applications/features and details about the investigations.

No.	Type of SMAs	Type of SPD Technique	Application/Feature	Ref.
1	Ti–Ni	Local canning compression	Amorphous structures	[56]
2	Ti–Ni	Local canning compression	Effect of the twins on the transformation behavior of the nanocrystalline NiTi	[57]
3	Ti–Ni	Local canning compression	Mechanisms of amorphization of NiTi SMA	[58]
4	Ti–Ni	High-pressure torsion	Structural investigations of nanostructured NiTi SMA	[59]
5	Ti–Ni	Equal-channel angular pressing	Viscoplastic FEM simulation, microstructural observation	[60]
6	Ti–Ni	High-pressure torsion Equal-channel angular pressing	Phase transformation sequence, microstructural studies	[61]
7	Ti–Ni	Equal-channel angular pressing	Phase transformation and precipitates' behavior	[62]
8	Ti–Ni	Equal-channel angular pressing	Martensitic transformations and effect of second phases	[63]
9	Ti–Ni	Equal-channel angular pressing	Transformation behavior and effect of pass numbers	[64]
10	Ti–Ni	Equal-channel angular pressing	Phase transformation, microstructural observation	[65]
11	Ti–Ni	Equal-channel angular pressing	phase transformations and superelasticity	[66]
12	Ti50–Ni50, Ti49.5–Ni50.5, Ti50–Ni49–Fe1	High-speed high-pressure torsion Equal-channel angular pressing	Phase transformation behavior	[67]
13	Ti–Nb–O	Equal-channel angular pressing	Superelastic behavior and precipitation effects	[68]
14	Ti–Mo	Equal-channel angular pressing	Martensitic transformations and effect of second phases	[63]
15	Cu–Al–Be–B	Equal-channel angular pressing	Microstructural observation	[69]
16	Cu–26Zn–5Al	Accumulative roll-bonding	Shape memory effect and phase distribution	[70]

Table 1. *Cont.*

No.	Type of SMAs	Type of SPD Technique	Application/Feature	Ref.
17	Cu–Zn–Ni	Accumulative roll-bonding	Martensitic transformation and SMA behavior, microstructural observation	[31]
18	Cu–Al–Mn	Accumulative roll-bonding	Microstructure, phase formation, corrosion	[71]
19	Cu–Al–Mn alloys Cu–9.5Al–8.2Mn Cu–8.3Al–8Mn	Accumulative roll-bonding Equal-channel angular rolling	-	[72]
20	Fe–Mn–Si	High-speed high-pressure torsion	Magnetism	[73]
21	Fe–Mn–Si	High-speed high-pressure torsion	Actuator	[55]
22	Ni50.5–Ti49.5	Constrained groove pressing	Biomedical	[34]
23	Ni57–Fe18–Ga25	High-speed high-pressure torsion	Amorphization and magnetism	[74]
24	Ni50.3–Ti49.7	High-speed high-pressure torsion	Smart hybrid material	[75]
25	Ni–Fe–Ga Ni57–Fe18–Ga25	High-speed high-pressure torsion	Smart hybrid material	[75]

2. Influence of SPD Processing on the Shape Memory Effect

One of the important features of SPD techniques is the intense grain refinement, which in turn can affect the shape memory properties and superplasticity. It has been reported that grain size could significantly affect the hysteresis loop area, martensitic transformation stress, and strain in Ni-rich NiTi alloys [76,77]. It can be expected that amorphization will also have a significant impact on the shape memory behavior. The reason behind the dependence of martensitic transformation on the crystal size is the atoms' movement during solid phase transformation, and its suppression by reduction in the crystal size [76]. Additionally, the grain and crystal size can substantially affect the morphology of martensite phases, and as it is known, the martensite morphology is of imperative significance for the macroscopic thermomechanical response of SMAs [78,79]. It was demonstrated that high-pressure torsion (HPT) processing of NiTi led to the formation of grain sizes less than 100 nm that caused intense suppression of the martensitic phase transformation, this transformation was even completely stopped in nanograins smaller than a critical size of 50 nm [76]. This phenomenon was attributed to the increase in the transformation energy barrier with a reduction in grain size, which finally leads to the decrease in the transformation temperature and its volume fraction [76]. Grain size reduction can also change the transformation path and decrease the thermal stability of the martensite. In brief, all of these procedures are due to size-dependent transformation barriers, including both elastic strain energy and twin boundary energy. For the case of superplasticity, it was shown that reaching grain sizes less than 100 nm can lead to superior superelasticity [80].

3. Effect of Different SPD Techniques on the Behavior of SMAs

3.1. Constrained Groove Pressing (CGP)

Among the various SPD methods, the constrained groove pressing process is one of the main techniques for the improvement of mechanical properties [81,82]. Figure 2 shows a schematic illustration of this process and the evolution of plastic strain during CGP. This technique can successfully change the microstructure of the Nitinol alloy from a mixture of austenite and martensite to stress-induced martensite in the first-pass CGP-processed sample, and later amorphization in the second-passes of the CGP process. It was also observed that there had been a significant change in the mechanical properties, i.e., yield strength by 170%, ultimate tensile strength by 160%, microhardness by 76%, and uniform elongation in the range of 50–80% [34]. In addition, CGP processing of Nitinol has been successfully shown to decrease the sub-grain size in the range of 74 to 104 nm. As can be

observed from the microstructure of the constrained-groove-pressed Nitinol shape memory alloy in Figure 3, water quenching at room temperature led to the fabrication of martensitic (sharp needle-like structure) and austenitic phases in the Nitinol shape memory alloy, along with a few examples of twinning. Twining resulted from the application of high thermal gradients and internal stresses during water quenching, and the low stacking fault energy of Nitinol. Another reason is the application of highly effective strains during CGP leading to the production of deformation, twinning, and shear bands, which eventually result in grain refinement, as seen after one pass and two CGP passes in Figure 3. Also, scanning electron microscopy (SEM) micrographs demonstrate the presence of sharp grain boundaries, Ti_2Ni particles (bright white spots), and needle-like martensite structures. These stress-induced martensite phases, fabricated from primary austenite phases, possibly contain dislocations and twinning. It is believed that the combined effects of precipitation, phase transformation, and dislocation density, due to the application of SPD techniques, leads to a stable, consistent, and improved superelastic response in Nitinol alloys [83].

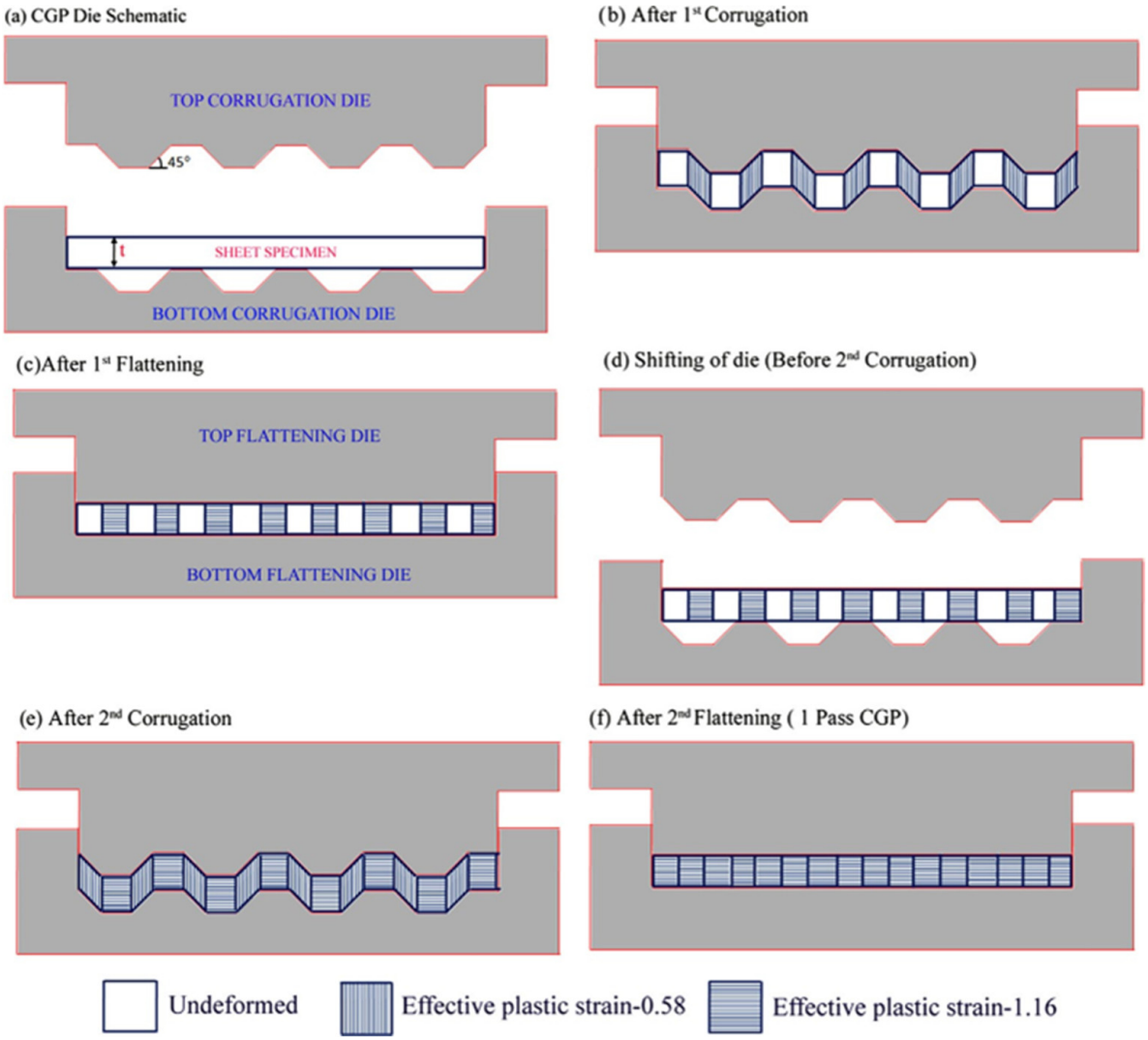

Figure 2. Schematic representation of the plastic strain evolution during the constrained groove pressing process, (**a**) CGP Die Schematic, (**b**) After 1st Corrugation, (**c**) After 1st Flattening, (**d**) Shifting of die (Before 2nd Corrugation), (**e**) After 2nd Corrugation, (**f**) After 2nd Flattening. Adapted with permission from [81], 2022, Elsevier.

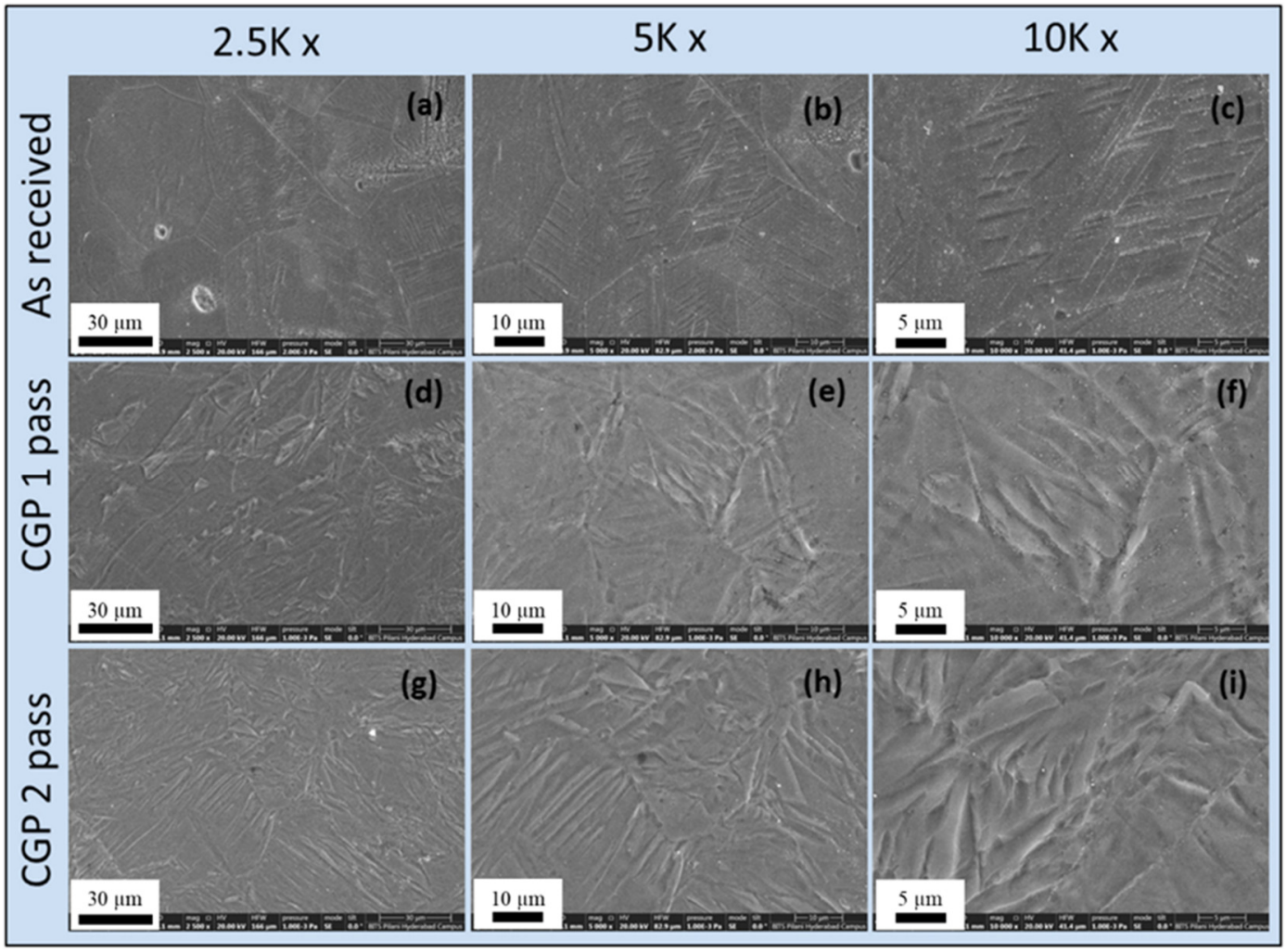

Figure 3. Scanning electron microscopy (SEM) images of (**a**–**c**) initial, (**d**–**f**) the first pass, and (**g**–**i**) the second pass of the constrained-groove-pressed Nitinol shape memory alloy at different magnifications, adapted with permission from [34], 2022, Elsevier.

The mechanical response of CGP-processed Nitinol samples after one and two passes is shown in Figure 4, demonstrating the sharp drop of elastic elongation, and serration with slight jumps in the plastic flow stress zone after one and two passes, indicating the occurrence of twinning. Twinning is mainly due to the formation of dislocations during cold deformation that promotes twinning growth at high strains [84–87]. Despite the significant drop in elongation after CGP processing, considerable improvements are observed in the yield and ultimate tensile strength that are attributed to the dislocations' rearrangement and activation of restoration mechanisms during the tensile test at high strains [34]. As is known, a dislocation forest can obstruct the dislocation glide and movement during the tensile test, leading to a reduction in plastic flow and enhancement of the yield strength [88].

3.2. Equal-Channel Angular Pressing/Extrusion (ECAP/E)

Equal-channel angular pressing (ECAP) was proposed and introduced by Segal et al. in the early 1970s, and developed rapidly thereafter [69,89,90]. One of the SPD technologies for grain refinement and producing UFG and even NS metals and alloys is ECAP. A schematic illustration of the ECAP process is shown in Figure 5. In this method, the extruded sample passes through a die containing two equal channels with an arbitrary angle. Therefore, the sample is subjected to extreme shear deformation in the die channels, leading to grain refinement. In the ECAP die, an internal channel is bent through an abrupt

angle, Φ, and there is an additional angle, Ψ, which represents the outer arc of curvature where the two channels intersect, shown in Figure 5. The sample, in the form of a rod or bar, is machined to fit within the channel, and the die is placed in some form of design, so that the specimen can be pressed through the die using a plunger. The imposed plastic deformation is simple shear. This method can allow large homogeneous plastic strains to be uniformly applied to the material while maintaining the same cross-sectional dimensions, which may be critical for industrial applications [87,91,92].

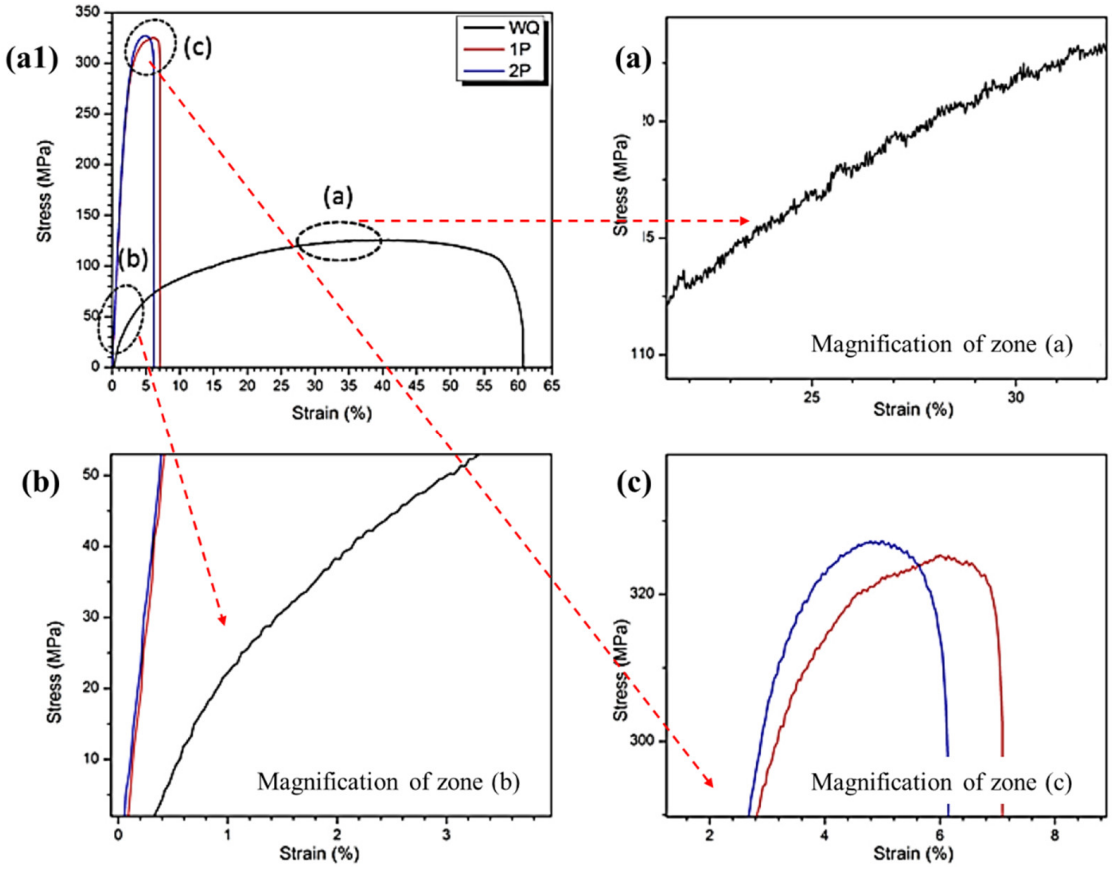

Figure 4. (**a1**) Stress-strain curve for initial, first-pass, and second-pass CGP-processed Nitinol samples indicating different zones of (**a**) magnification of zone (a) showing plastic region with the deformation twinning in water-quenched condition, (**b**) magnification of zone (b) showing an elastic region of the tensile testing sample, and (**c**) magnification of zone (c) showing the plastic region and the onset of twinning in the first- and second-passes, adapted with permission from [34], 2022, Elsevier (WQ means water quenching).

As known, grain refinement improves the functional and mechanical properties of SMAs, and the ECAP technique, providing sufficient grain refinement, can improve SMAs' mechanical responses. Additionally, the shape memory behavior and superelasticity of SMAs are influenced significantly by their microstructure. In order to optimize the microstructure of TiNi, various SPD methods have been developed. The ECAP method is mainly used for grain refinement, to upscale and process difficult-to-deform materials. The importance of microstructures developed by the ECAP technique in single-crystal and polycrystalline materials, with single and multiple phases, has been widely investigated so far. The emergence of UFG, and even NS, in materials are responsible for a significant improvement in their physicomechanical properties. However, it has been shown that to achieve enhanced properties after ECAP processing, a wide range of microstructural factors, such as grain boundaries, misorientations, crystallographic texture, and the distribution of any second phases, should be controlled [4].

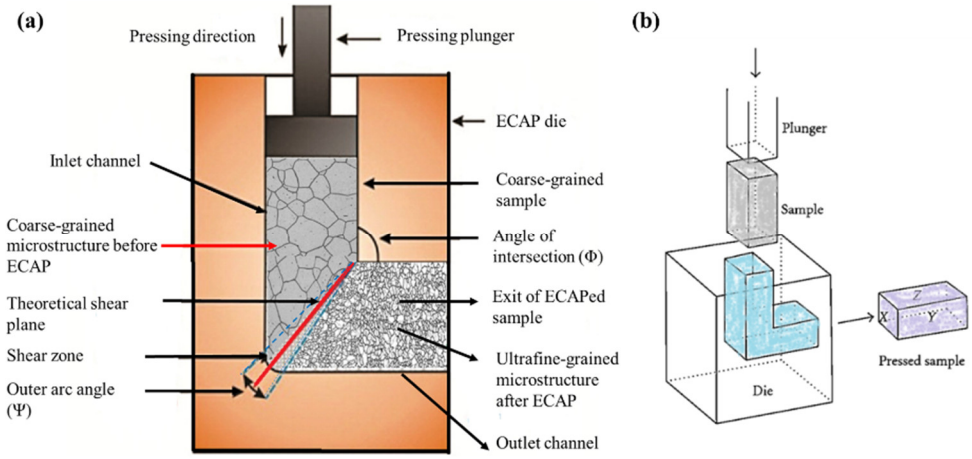

Figure 5. A schematic illustration of the ECAP process: (**a**) the different parts of the ECAP die, channels, angles, and shear zone, and (**b**) the sample passing through the ECAP channels.

An experimental study conducted by Arockiakumar and Park [68] proved that the superelastic response of an ECAPed Ti–40Nb–0.3O (wt.%) alloy was recovered after post-annealing. They reported a reduction in the superelastic strain of 2.0–2.5%, due to the decrease in the elastic strain, and precipitation of the α phase, which led to oxygen depletion in the β matrix. Post-annealing of ECAPed samples in a two-phase (α + β) structure leads to the fabrication of a fine recrystallized grain structure, with an average grain size of ~1 µm. The superelastic strain and its transformed post-annealed ECAPed sample were enhanced in the early stages of annealing, dropped in the next stage, and eventually reached their peak at an intermediate annealing time [68].

In another study, the equal-channel angular rolling (ECAR) method was performed successfully on a Cu–8.3Al–8Mn alloy, up to five passes at room temperature, followed by post-annealing at 890 °C for different lengths of time. The ECAR method, as one of the severe plastic deformation processes, is very similar to the ECAP method, except it utilizes rolling instead of pressing or extrusion. ECAR is suitable for shear deforming long and thin sheets continuously; it should be noted that the thickness of a sheet is not reduced during ECAR. According to scanning electron microscopy (SEM) studies, the coexistence of bainitic and martensitic structures is the main reason for the improvement in the mechanical properties of the ECARed Cu–8.3Al–8Mn alloy [72]. It was noticed that the mentioned process improved the tensile properties of the Cu–9.5Al–8.2Mn alloy, which is attributed solely to grain refinement. After post-deformation annealing, the transformation temperature was reduced in both alloys, and the specific growth of martensite variants occurred [72]. In this regard, Figure 6 shows the microstructure, tensile properties, and fracture surfaces after the tension. According to Figure 6a, the fracture surface of the as-received sample has hollow and equiaxed dimples, as is clear in the magnified inset, while the five-passes ECARed sample (Figure 6b) shows a ductile fracture with deep dimples, clearly seen in the magnified inset subfigure. Additionally, Figure 6c indicates the SEM micrograph of the five-passes ECARed sample after heat treatment, including martensitic phases, fabricating during quenching, and some plate-like β precipitates. Figure 6d shows the mechanical performance of the samples in different states and martensitic conditions. After annealing, the processed alloy has deeper and closer dimples, indicating improved mechanical characteristics. Moreover, after post-deformation annealing on the ECARed Cu–Al–Mn SMA samples, transformation temperatures decreased, and selective growth of martensite variants was observed [72].

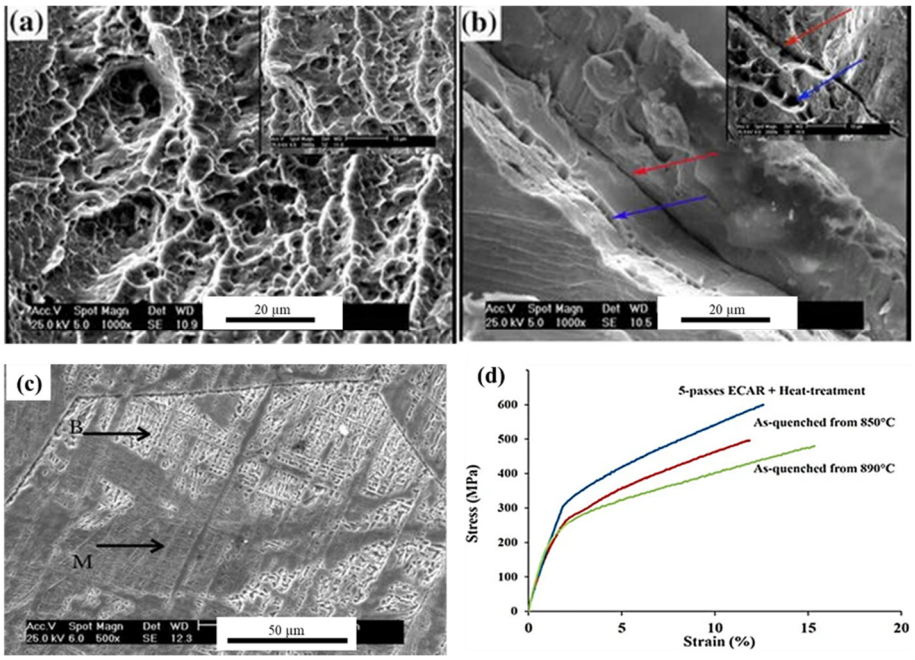

Figure 6. Cu–8.3Al–8Mn alloy after five passes of the ECAR process and post-deformation annealing, (**a**) fracture surface after the tensile test for the as-received sample, and (**b**) five-passes ARB and heat-treatment; (**c**) SEM microstructure after five passes of ECAR and post-deformation annealing heat treatment including β grains and martensite; (**d**) room-temperature stress-strain curves under different processing conditions, adapted with permission from [72], 2022, Springer Nature.

Cu-based SMAs have been investigated thoroughly due to their cost-effectiveness, acceptable shape memory effect, high pseudoelasticity, and damping characteristics. However, their lack of ductility and thermal stability have limited their applications. Previous findings have revealed that such flaws are related to the microstructure feature of Cu-based SMAs, including a coarse grain size, strong elastic anisotropy, and the buildup of impurities at grain boundaries [93,94]. Applying the ECAP process fabricates equiaxed ultrafine grains (grain size of ~2 µm) with a decreased martensite percentage. The development of martensite (18R) and finer grains are accelerated through the quenching process. Although the percentage and ratio of martensite increase significantly, the coarsened grains (~50 µm) remain thinner than those in the as-received samples (100–300 µm) [69].

TiNi alloy is being utilized in a wide range of applications due to its excellent shape memory effect and superelastic characteristics. The ECAP technique has been widely applied to TiNi SMAs, developing its application range due to the improved mechanical properties, microstructure evolution, and phase transformations [62,66]. Finite element modeling (FEM) was employed to calculate the stress, strain, and velocity fields of the TiNi SMA tube, showing that the plastic deformation of the inner corner is greater than that of the outer corner in the real strain field. After applying ECAP on a TiNi SMA tube, the velocity field results reveal that particle flow is obstructed in the corner. Also, with one extrusion pass, the microstructural modification of the TiNi SMA tube is minimal [60]. It is generally accepted that the ECAP method is an essential SPD approach to improving a material's microstructure through significant shear plastic strain, leading to microstructure refinement in TiNi SMAs down to about 250. This method can also help to improve yield strength, tensile strength, maximum reaction stress, and recoverable strain of the material [61]. It should be noted that hard-to-deform materials like TiNi-based intermetallic alloys require elevated temperatures to be processed by ECAP; Figure 7 shows bright-field TEM micrographs of a $Ti_{49.4}Ni_{50.6}$ alloy after the ECAP process at 400–500 °C. The microstructure includes equiaxed grains with an average grain size of 200–300 nm, fine grains with mean grain sizes of less than 200 nm, and lattice dislocations. It is observed in

Figure 7c that annealing at 550 °C led to an increase in the grain sizes, up to 500–600 nm, also the grain boundaries became straight and sharp along with a reduction in lattice dislocations [61].

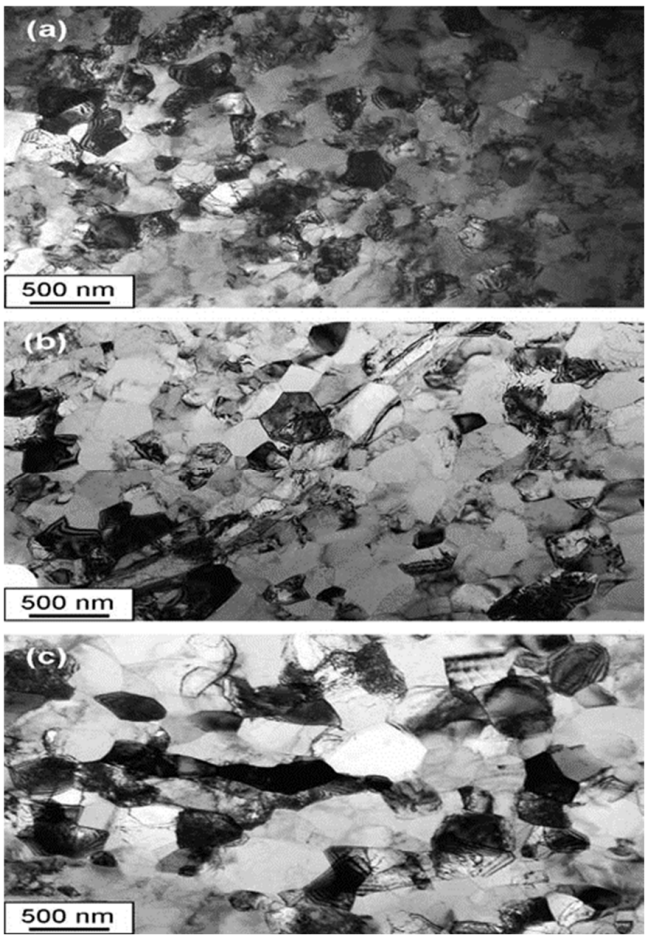

Figure 7. Bright-field TEM micrographs of the $Ti_{49.4}Ni_{50.6}$ alloy processed by the ECAP method at (**a**) 400 °C for eight passes, (**b**) 500 °C for twelve passes, and (**c**) 450 °C for eight passes and subsequent annealing at 550 °C for 1 h, adapted with permission from [61], 2022, Elsevier.

The ECAP process has advantages for bulk materials due to the refined microstructures, resulting in ultrafine grains, high dislocation density, and a higher volume fraction of high-angle grain boundaries (HAGBs). The fine microstructures and energy buildup caused by this method are related to the $B_2 \rightarrow R$ phase transition. High-density dislocations and grain boundaries result in a lower-energy R-phase production [62]. In a previous study, it was noted that after eight passes of the ECAP process, the coarse grains of a Ti–50.9at%Ni sample were considerably refined. With the ECAP method at 773 K, the R-phase transformation is accelerated, and the martensitic temperature is reduced compared to Ti–50.9at%Ni. The submicron-grained Ti–50.9at%Ni alloy demonstrated a significant shape memory effect and superelasticity [64].

3.3. High-Speed High-Pressure Torsion (HSHPT)

High-speed high-pressure torsion (HSHPT), a variant of the HPT process with superb rotational speed, is one of the severe plastic deformation techniques [95]. During the HSHPT process, the material is subjected to the simultaneous application of high compressive pressure and torsion, it should be noted that torsion is conducted by the high rotational speed of the upper anvil. Figure 8 shows the HSHPT technology along with its anvils, samples, and machine [96].

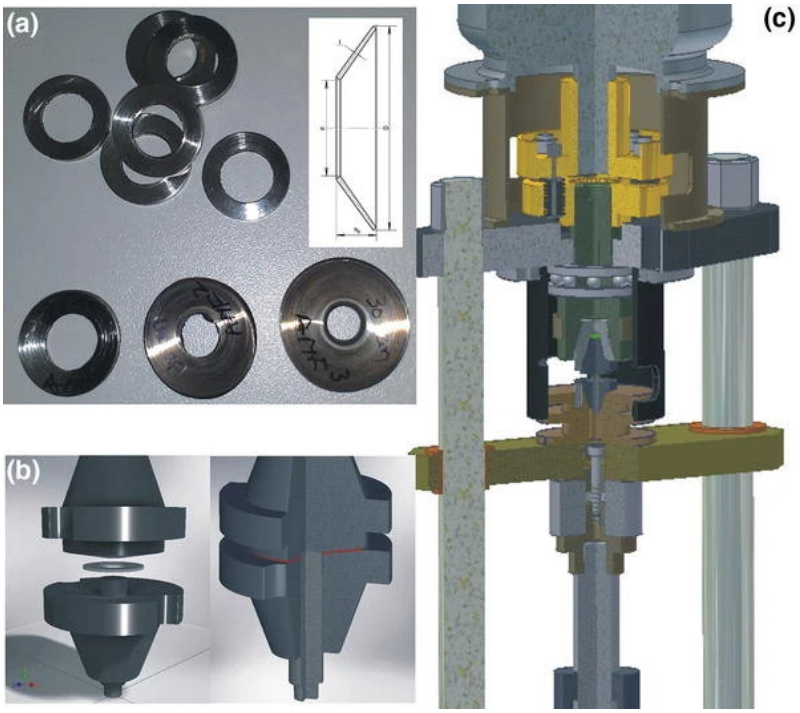

Figure 8. HSHPT technology: (**a**) disk-shaped samples and their geometry, and final shapes of Fe–Mn–Si–Cr SMA coned disk spring-shape modules, (**b**) HSHPT upper and lower anvils with open and closed conditions, and (**c**) HSHPT machine, adapted with permission from [96], 2023, Springer Nature.

The effect of the HSHPT process on the morphology and magnetic properties of the shape memory $Ni_{57}Fe_{18}Ga_{25}$ Heusler alloy was investigated thoroughly. The main structural characteristic of the Heusler alloys is their ordered structure, with an FCC superlattice and a BCC unit cell [53,54]. The first sample crystalline structure of the shape memory $Ni_{57}Fe_{18}Ga_{25}$ Heusler alloy appears biphasic at room temperature, with an L10 tetragonal and a cubic gamma phase. Moderate imposed deformations affect the ratios of different phases and cause grain size reduction and phase rearrangement. Decreasing the grain size of the sample leads to a significant drop in the martensitic transformation temperature and the behavioral pattern of the magnetic properties, such as the Curie temperature, saturation magnetization, and coercive field, which decrease when the applied deformation level is increased [74]. Figure 9 shows the microstructure evolution, the temperature dependence of magnetization, and the magnetization thermal variation for the $Ni_{57}Fe_{18}Ga_{25}$ Heusler alloy, with shape memory effect after the HSHPT method. The samples were processed by the HSHPT machine, with a hydrostatic pressure of about 1–1.3 GPa, by three subsequent turns, using a rotation speed of the upper anvil of about 900 rpm. The samples were categorized according to their strain values, including (ini) for the initial sample, SPD_1 for $\varepsilon = 0.9$, SPD_2 for $\varepsilon = 1.74$, and SPD_3 for $\varepsilon = 2.82$ (where ε is the strain value). It should be noted that the deformation degree and strain values were calculated by $\varepsilon = \ln(h_i/h_f)$, in which ε is strain value and h_i and h_f denote the initial and final thicknesses of the sample, respectively. The microstructure includes γ phase precipitates embedded in a β martensite matrix (Figure 9a); such a dual microstructure was also shown in Ni–Fe–Ga magnetic shape memory alloys after HSHPT processing [97]. Further microstructural analysis with SEM demonstrated martensite plates inside grain boundaries, with fine and diamond-like morphology, shown in Figure 9(b1) with $\varepsilon = 0.9$, while γ precipitates located at the matrix grain boundaries. For the case of the SPD_2 sample, with $\varepsilon = 1.74$, shown in Figure 9(b2), no grain boundaries can be clearly seen, and secondary-phase precipitates manifested a significant ordering and fragmentation, which can be seen with more detail in Figure 9(b3). In the SPD_3 sample, with $\varepsilon = 2.82$,

shown in Figure 9(b4), a heavily deformed microstructure was observed, with curved fibers, implying that the application of high compression and torsion led to severe grain refinement by shearing, and the fabricated grains of secondary-phase precipitate or grain boundaries are highly refined and so are not detectable with electron microscopy [74]. The thermomagnetic curves of the HSHPT-processed $Ni_{57}Fe_{18}Ga_{25}$ shape memory alloy are shown in Figure 9(c1,c2), it is seen that the magnetization has a straightforward relation with an increasing degree of deformation. This magnetization improvement in the M_T curves of the SPD_1 and SPD_2 samples is attributed to the increase in the cubic γ phase amount. As the M_T takes place at $\geq T_C$ (Figure 9(d1,d2)), the $Ni_{57}Fe_{18}Ga_{25}$ alloy is considered a simple shape memory alloy with partially ferromagnetic martensite. The SPD technique influences the properties of this material by modifying the crystallite dimensions and adjusting the magnitude of the gamma secondary phase.

Sergueeva et al. investigated the production of nanocrystalline amorphous TiNi through the combination of aging and the high-pressure torsion (HPT) method. Nanocrystallization of amorphous NiTi samples using the HPT method led to the formation of homogeneous nanocrystalline microstructures with different grain size ranges, and with a much higher strength than the microcrystalline state. The highest elongation, of 120%, was observed at elevated temperatures, and the ultimate tensile strength, of over 2.5 GPa, was detected at ambient temperature [95]. In another study, it was found that high-quality bonding between two alloys of NiTi SMA and a Ni–Fe–Ga Heusler alloy is possible by the HSHPT method, the fabricated layers are well-coordinated, and there is no interfacial intermediate layer development. The resultant two layers of the hybrid material produce a sub-microcrystalline structure. The findings demonstrate that the HSHPT method may be used to make bilayer and multilayer TiNi/Heusler alloy composites [75]. The grain refinement processes that lead to the ultrafine-grained (<1000 nm) and nanocrystalline NC (<100 nm) structures have a quite complex mechanism, and require a long-range redistribution in various parts of the sample. Although, in the instance of an exceedingly brittle state at low temperatures, coarse grain size, or as-cast alloys, the use of the SPD method results in an extraordinarily high strength and hardness, as well as low-temperature superplasticity [98,99]. By using the SPD techniques, a fundamental martensitic change and magnetic characteristics are achievable.

Gurau et al. [73] investigated the relationship between magnetic properties and severe plastic deformation in Fe–Mn–Si–Cr shape memory alloys. Thermomagnetic curves between 150 and 390 K, and magnetic hysteresis loops at 300 K have been measured. The thermo-resistivity experiments were performed using a four-probe system. Also, the magnetic characteristics were analyzed and compared with the obtained microstructure for Fe–Mn–Si–Cr SMA. HSHPT fabricates plate-shaped martensite needles (50 to 120 nm) and many stacking faults in Fe–Mn–Si–Cr SMAs [73]. It was also found that the antiferromagnetic behavior is directly dependent on the austenitic γ phase evolution and magnitude. The Fe–Mn–Si–Cr alloy produced by the HSHPT method does not have the high density of dislocations or amorphous regions that are typical in SPD-processed materials. The crystallized martensitic structure could be employed for industrial actuator applications. Note that no post-deformation annealing is required following HSHPT [55]. Also, a uniform structure is produced during the HPT processing of large samples, with rarely spaced nanocrystallites maintained within the amorphous phase. Simultaneously, the B_2-austenite nanocrystalline grains continue to be larger in the core region, while the volume percentage of the amorphous phase decreases. Thin discs practically undergo comprehensive amorphization when the HPT circumstances are equivalent in terms of total complete revolutions and pressure, which is shown by the increased degree of shear deformation in these samples [59]. Figure 10 shows the microstructure evolution of an Fe–Mn–Si–Cr alloy after the HSHPT method. After the application of 1.53 strain, as seen in Figure 10a, the microstructure shows the presence of ε martensite plates, γ austenite, and a small amount of α' martensite (body-centered tetragonal). Also, the SAED pattern in Figure 10b shows the coexistence of two plate-like ε martensite variants. Moreover, a

combination of very fine plates (50 to 120 nm) and twin colonies of ε martensite plates is detectable in the TEM micrograph of an SPDed Fe–Mn–Si–Cr alloy after 1.71 strain, Figure 10c. These colonies include numerous finely spaced parallel plates (<10 nm thick), with the existence of many stacking faults in the austenitic phase (Figure 10c). It should be noted that the existence of ε martensite is imperative for the generation of the shape memory effect in Fe–Mn–Si SMAs, and the reduced stacking fault energy of the austenite facilitates the formation of martensite. The HSHPT application separated the intersecting martensite plates and variants, resulting in the generation of at least two parallel banded reliefs along two different directions, originating from ε_{hcp} stress-induced martensite habit planes, Figure 10d [73].

3.4. Local Canning Compression (LCC)

Among the various SPD methods, local canning compression (LCC) is one of the most used methods in the industry. Local canning compression (LCC) is a well-known method in the plastic deformation of SMAs. A schematic representation of this process is given in Figure 11. Accordingly, a cylindrical sample is first extracted from the as-received SMA bar along the axial direction, through electro-discharge machining. After that, the sample is locally canned by a ring-shaped steel can, so that the can is placed in the mid-height of the sample based on interference fit. Note that the steel cans are generally made of low-carbon steel. Eventually, the canned SMA sample is compressed up to the desired strain value through the universal testing machine, and then the steel can is removed from the compressed SMA sample [100,101]. A schematic representation of the LCC process is shown in Figure 11a, along with the nanocrystallization and amorphization mechanisms for the TiNi sample under local canning compression, in Figure 11b. In the amorphization and nanocrystallization procedure of TiNi SMA by the LCC technique, deformation twinning and dislocation slip seem to be of particular importance. Following the SPD of TiNi SMA under the local canning compression method, stress-induced martensite transformation develops, and the stress-induced martensite reverses after unloading. Due to the mechanical stability of the stress-induced martensite, caused by the high plastic strain and stress fields, the preserved nanocrystalline phase in the TiNi sample that is subjected to the intense plastic deformation forms B_2 austenite and $B_{19'}$ martensite. Note that stress-induced martensite transformation, deformation twinning, dislocation slip, nanocrystallization, and amorphization are all part of the TiNi SMA's deformation mechanism when it is regionally compressed. Stacking faults and (001) martensite compound twins arise after the plastic deformation of TiNi SMA. The main deformation bands, secondary deformation bands, and amorphous bands coexist in the TiNi matrix as the plastic strain increases [56]. Figure 11b schematically shows the mechanism of nanocrystallization and amorphization of the TiNi sample under the LCC method. Furthermore, the deformation bands of the TiNi sample subjected to 50% deformation are shown in this figure. Accordingly, the deformation and amorphous bands of the TiNi sample which undergoes 75% deformation are detectable through TEM, shown in Figure 12, [50]. This issue implies that martensite twins are difficult to remove under 3D compressive stress conditions, even with substantial plastic strain. Simultaneously, the (001) compound twin is generated as a result of the deformation twinning of the martensitic TiNi sample. The type II twin is still captured in the annealed TiNi samples at 300 °C, which is attributed to the type II twinning-detwinning in the solution-treated TiNi sample. The retained deformation twin, due to plastic deformation of the initial TiNi alloy, is observable in the samples annealed at 450 °C, leading to the (001) compound twin. In the TiNi samples annealed at 600 °C, both (001) compound and type II twins can be detected, resulting from crystallization in new grains. TiNi SMA undergoes a one-stage phase transformation as a result of plastic deformation under the LCC method, during heating and cooling after annealing at 300 and 450 °C, with the corresponding martensitic transformations being directly related to the retained twins or retained coarse grains [57].

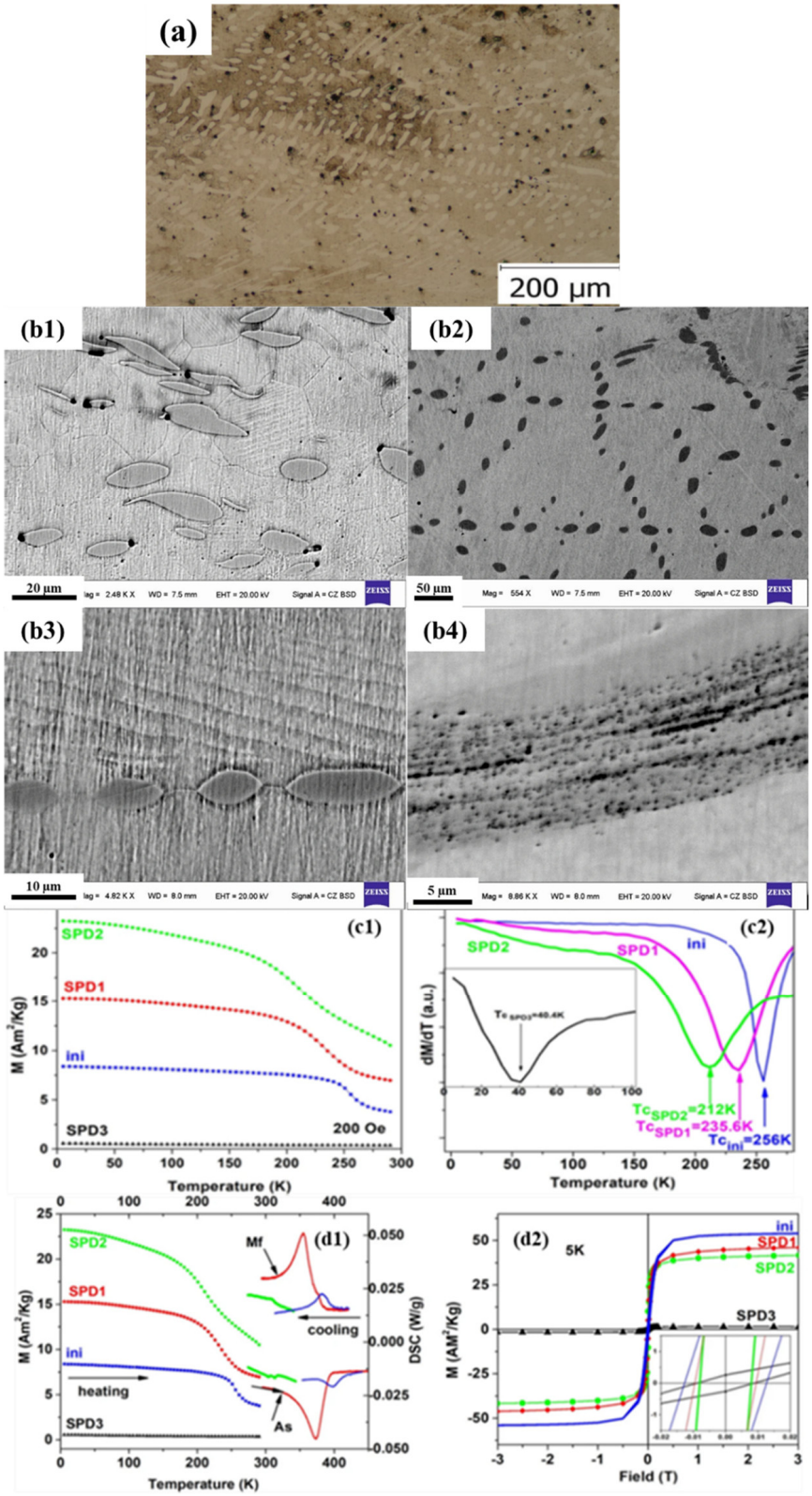

Figure 9. Microstructure evolution (**a**), (**b1**–**b4**), the temperature dependence of magnetization (**c1**,**c2**), magnetization thermal variation (**d1**), and DSC micrograph (**d2**) of the $Ni_{57}Fe_{18}Ga_{25}$ disc subjected to the HSHPT process, adapted with permission from [74], 2022, Springer Nature. Note that the Curie temperature (T_C) is evaluated from the first derivative of temperature-dependent magnetization. Also, hysteresis curves are measured at 5 K. The HSHPT samples are categorized into four groups, namely, (ini) for the initial sample, SPD_1 for $\varepsilon = 0.9$, SPD_2 for $\varepsilon = 1.74$, and SPD_3 for $\varepsilon = 2.82$.

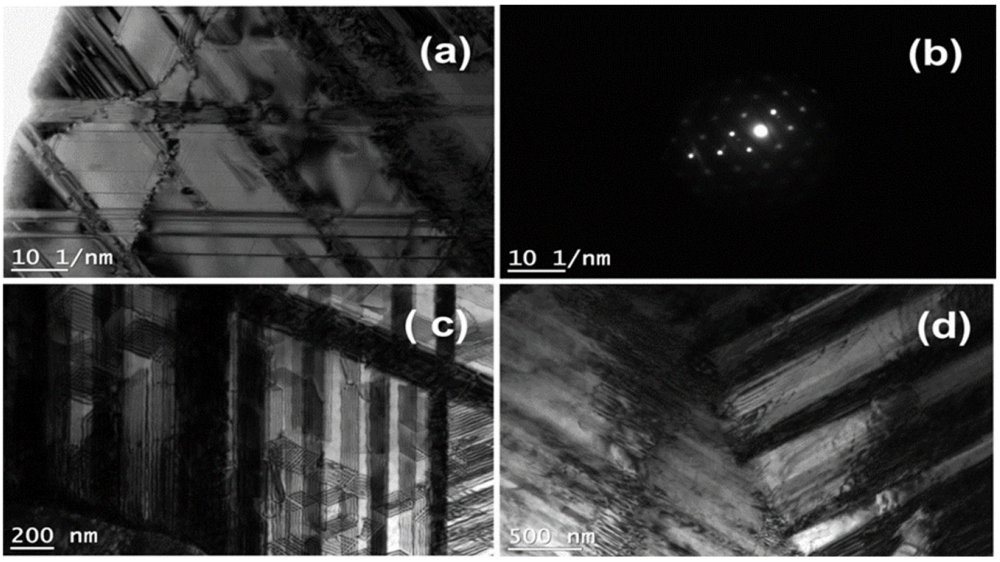

Figure 10. TEM observation of Fe–Mn–Si–Cr alloy processed by the HSHPT method with different degrees of deformation: (**a**) 1.53 strain, (**b**) SAED of (**a**), and (**c**,**d**) 1.71 strain, adapted with permission from [73], 2022, Trans Tech Publications, Ltd.

During LCC processing of NiTi samples, and plastic deformation of martensite NiTi samples, firstly, in order to accommodate the preferential orientation of applied external loading, the martensitic variants are reoriented and moved, usually fabricating a unified variant boundary [57]. After the martensitic reorientation process is finished, detwinning occurs in the martensite. An increase in the plastic strain led to the occurrence of deformation twinning in the local region, without twins that induce dislocation slip. As a result of all these steps, the grains are continuously and repeatedly refined, with successive increases in plastic strain. Finally, the dominant amorphous phase emerges along with the retained nanocrystalline grains [57]. A similar phenomenon was observed and reported by Nishida et al. [102]. It has also been shown that plastic strain localization in shear bands can lead to amorphization up to an area fraction of 90%, and crystal refinement down to 5 nm [103,104]. Other studies reported that plastic deformation in grain boundaries is the main reason for irrecoverable strains, while the amorphous phase and twins cause high-stress levels and the disappearance of the stress plateau [105]. Also, the simulations, using large-scale molecular dynamics, demonstrated the significant importance of anisotropy in martensite generation [106].

During the annealing procedure of the LCCed NiTi sample, at temperatures ranging from room temperature to 800 °C, a Ni-rich NiTi SMA, which was in the austenitic condition at ambient temperature, was subjected to plastic deformation via the LCC method [57]. Several plastic deformation mechanisms have been observed in NiTi SMA depending on temperature, including dislocation slip, deformation twinning, grain boundary slide, grain rotation, dislocation climb, and grain boundary migration. Accordingly, amorphization, dynamic recovery, and dynamic recrystallization can be identified at different temperatures. To this end, dislocation slip and deformation twinning were applied separately to examine the mechanism of localized amorphization. The amorphization of the obtained NiTi SMA was affected by statistically stored dislocations (SSD) and geometrically required dislocations (GND). NiTi SMA appeared to have a specific dislocation density beyond which it could not be amorphized. As a result, there will be a critical temperature for a constant deformation strain, in which the NiTi SMA matrix will not form an amorphous phase. When a TiNi SMA is subjected to plastic deformation at a critical temperature, amorphization and crystallization occur simultaneously and compete with each other [58].

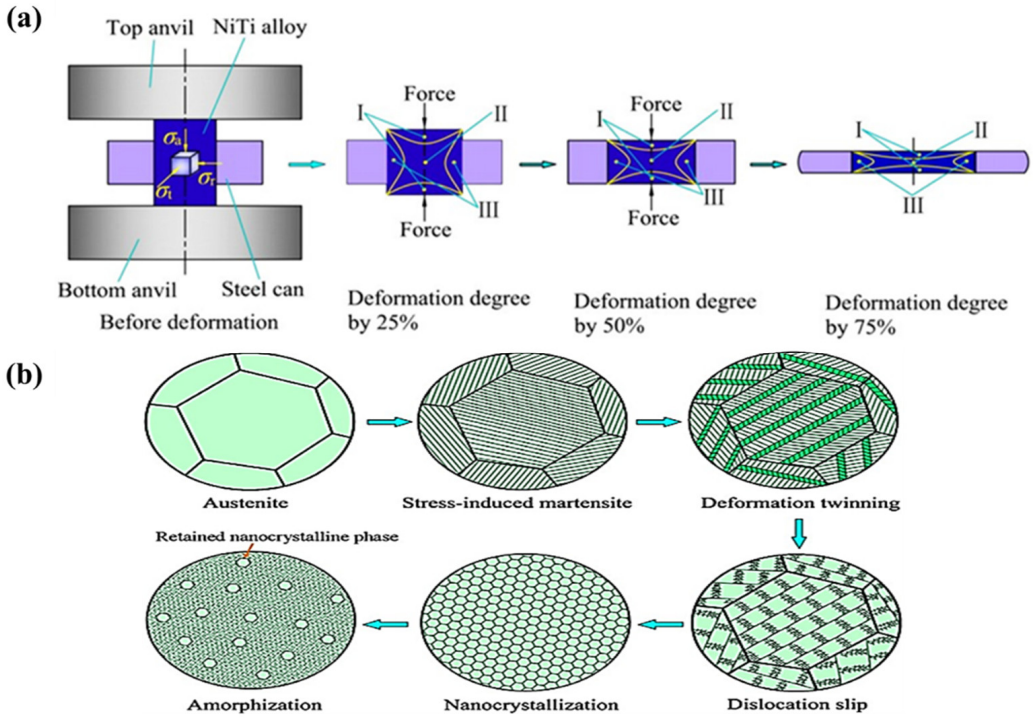

Figure 11. (**a**) Schematic representation for the local canning compression processing (region I shows the minimum deformation zone, region II illustrates the main deformation zone, and region III depicts the intermediate deformation zone) [56], and (**b**) nanocrystallization and amorphization mechanism for the TiNi sample under local canning compression, adapted with permission from [56], 2022, Elsevier.

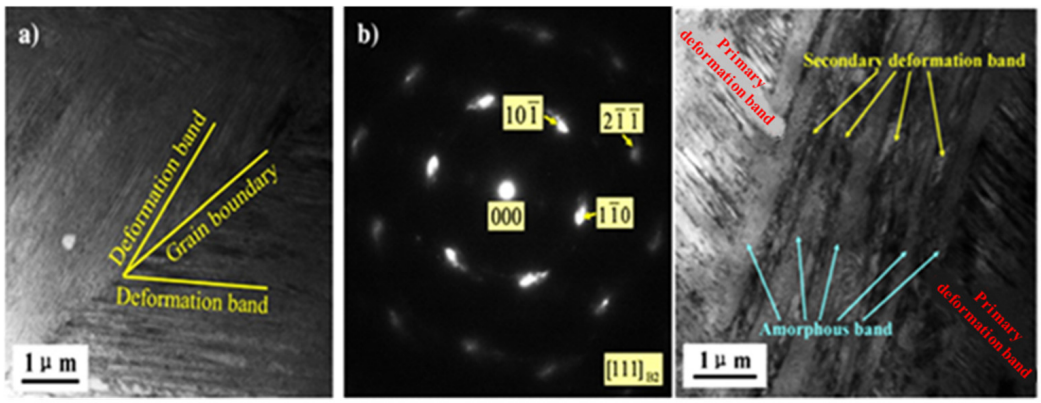

Figure 12. The nanocrystallization and amorphization mechanism for the TiNi sample under local canning compression in which the deformation bands of the TiNi sample were subjected to 50% plastic deformation, where (**a**) bright-field TEM image showing the deformation bands next to the grain boundary and (**b**) SAED pattern showing B_2 austenite structure, adapted with permission from [56], 2022, Elsevier.

3.5. Accumulative Roll-Bonding (ARB)

Accumulative roll-bonding is a method of severe plastic deformation that involves rolling a stack of materials, sectioning it into two halves, collecting it back up, and rolling it over and over again to form an ultrafine-grained structure, as illustrated in Figure 13. The fabrication of lightweight high-strength materials is of great significance in several industries, such as aerospace, automotive, and biomedical, where the ARB method is a potential SPD process capable of fabricating UFG, and even NS, conditions throughout the final sample microstructure [9,107]. During ARB processing of SMAs, extreme grain

refinement, nanostructuring, and amorphization can lead to a superior superelasticity response. Lim et al. [108] proved that the application of high-ratio differential speed rolling (HRDSR) as one of the SPD techniques led to the production of a nanograined structure (20–70 nm) composed of austenite and martensite nanograins and sub-nanograins, showing superior superelasticity. They implied that the heavily deformed austenite and martensite produced, and an amorphous phase, were the result of a discontinuous static recrystallization process in which detwinning, rather than the stress-induced martensite transformation, determined the final microstructure [108]. The ARB-processed Cu–26Zn–5Al alloy showed a significant strength and ductility of about 500 MPa and 22%, respectively. By increasing the temperature, the shape recovery ratio was enhanced until the ideal starting point was equal to 75% of the SME degree. Furthermore, the alloy manifested proper strength values after annealing at 900 °C. According to the findings, Cu–Zn–Al shape memory alloys may be especially effective when combined with accumulative roll bonding and subsequent heating treatment procedures [70]. Figure 14 shows a schematic representation of the bending tests for determining the strain recovery effect. Also, Figure 15(a1,a2) presents the OM images of the wear track; and Figure 15(b1,b2)) the SEM observation of the worn surface in the Cu–26Zn–5Al alloy. In a research study in Ref. [63], the ARB-processed nanostructured Cu–Al–Mn composite was found to have a matrix crystallite size of about 30 nm. No new phases were identified in the rolled composites after nine cycles. Also, the temperature had a significant impact on the microstructure and phase formation. When the heat treatment temperature was increased from 850 to 950 °C, the multiphase structure became a single-phase structure. For better results in the fabrication of Cu–Al–Mn alloys, ARB with solid-solution treatment is preferable [71]. Besides, Figure 15 represents the SEM image of the Cu–Al–Mn composite after nine cycles (Figure 15(c1)), the corresponding elemental maps (Figure 15(c2–c4)), and the point spectrum of the Cu/Al/Mn composite (Figure 15d) [70].

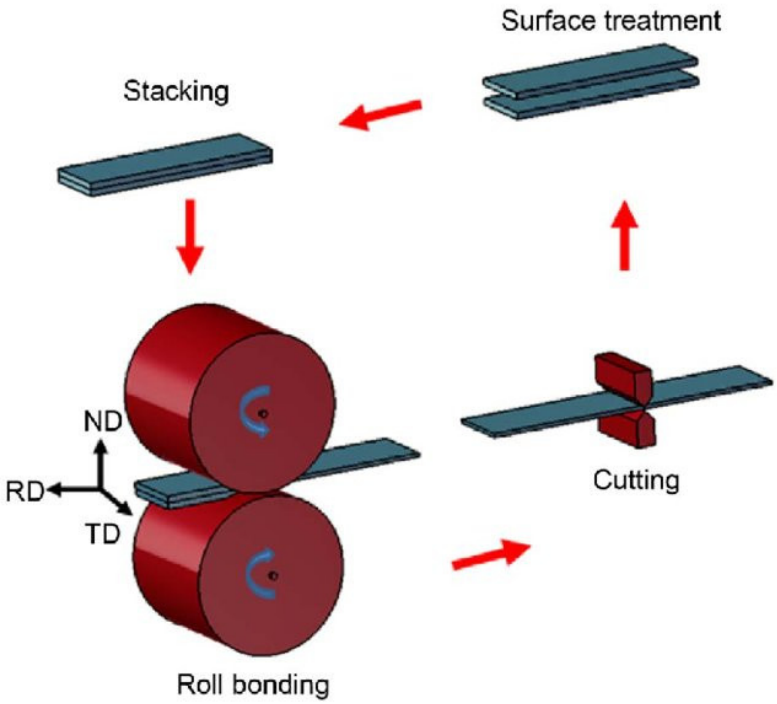

Figure 13. Schematic illustration of the accumulative roll-bonding (ARB) technique, adapted with permission from [109].

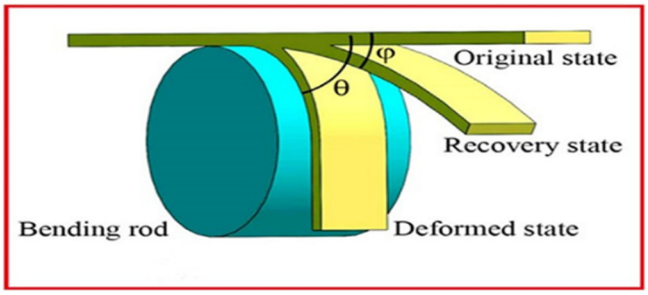

Figure 14. Schematic representation of the bending test to determine the strain recovery effect, adapted with permission from [70], 2022, Elsevier.

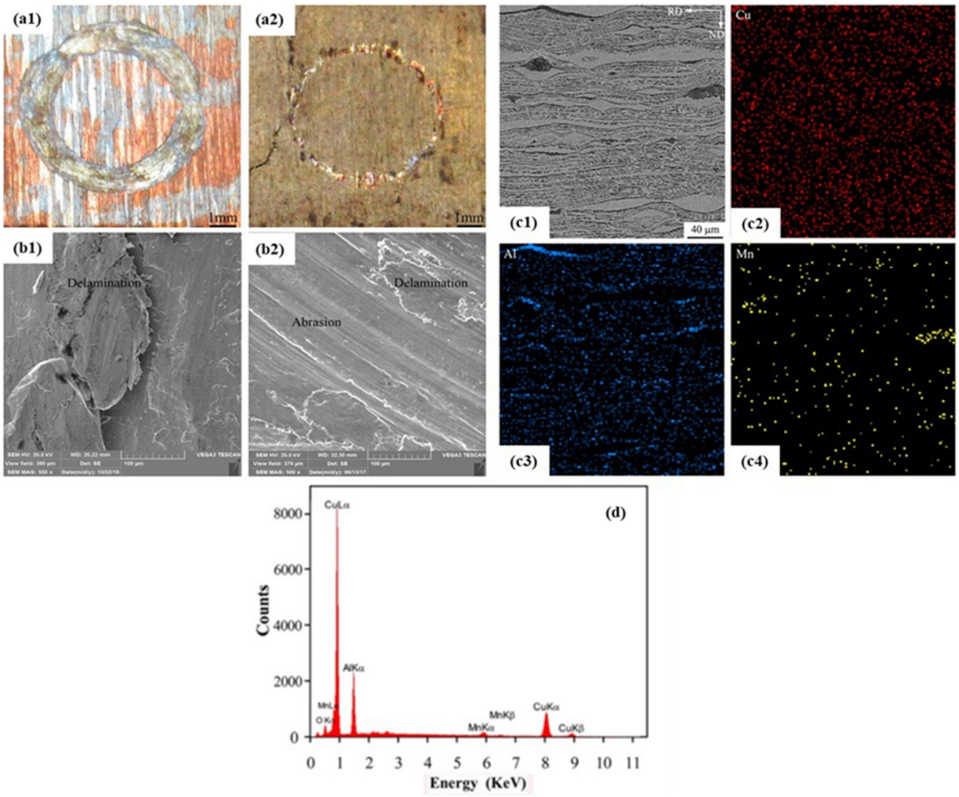

Figure 15. The ARB processed Cu–26Zn–5Al shape memory alloy, the wear track of (**a1**) Cu/26Zn/5Al multilayered composited material and (**a2**) Cu–26Zn–5Al alloy; SEM micrograph of the worn surface (**b1**) Cu/26Zn/5Al multilayered composited material and (**b2**) Cu–26Zn–5Al alloy [70]. (**c1**) SEM micrograph of Cu/Al/Mn composite after nine cycles and the related SEM elemental distribution maps for (**c2**) Cu, (**c3**) Al, (**c4**) Mn, and (**d**) point spectrum of the Cu/Al/Mn composite, adapted with permission from [71], 2022, Elsevier.

4. Conclusions and Future Remarks

Shape memory alloys, as unique materials for numerous industrial and medical applications, attract much attention, but they still should be improved, from a strength and toughness point of view, to meet all the requirements for application in higher-strength structures. Application of severe plastic deformation techniques, having the capability to extremely refine the microstructure and enhance the mechanical properties, is among the most promising options to improve the overall performance of various shape memory materials, and can be regarded as an excellent candidate for a new generation of advanced and modern shape memory alloys with high-throughput performance. Investigations have shown that SPD application on SMAs, leading to extreme grain refinement, can improve

mechanical and physical properties, including yield strength, ultimate tensile strength, hardness, fatigue endurance, corrosion, electrical resistance, thermal conductivity, friction and wear behavior, and damping. Additionally, SPD application can affect the distribution of phases, microstructural evolution, texture, twins' activity, phase transformation behavior, tribology, precipitation behavior, martensitic transformations, etc. Therefore, it is of eminent importance to investigate and discuss the exact influence of SPD processing via different techniques on various SMAs. Due to these numerous consequences of SPD processing, it has the potential to affect the shape memory effect and superelasticity, since grain refinement can affect the hysteresis loop area, martensitic transformation stress, and strain. The main reason for changes in the shape memory effect and martensitic transformation due to grain refinement, is related to atoms' movement during the solid phase transformation, and its suppression by a reduction in the crystal size. Also, the grain and crystal size can substantially affect the morphology of martensite phases, which can change the macroscopic thermomechanical response of SMAs. Also, magnetization can be improved, since SPD can affect the coercivity and Curie temperatures as a result of the grain size reduction. Moreover, severe straining through SPD methods can lead to nanostructuring and even amorphization. Various SPD techniques can lead to different properties and structures, they can also lead to the fabrication of multilayered composites with unique properties. Hence, studying the response of shape memory alloys to the application of different types of SPD methods is considered important, and in this research, we have examined the different methods and their effects on the different properties of SMAs.

It should be noted that post-processing heat treatment procedures play a key role, and SPD and subsequent aging contribute to raising the martensite transition temperature. SPD methods can also prevent the R-phase formation and different phase precipitates in NiTi SMA. The stress-strain curve of nanocrystalline/amorphous NiTi samples demonstrates an unusual pseudoelasticity, without a stress plateau and hysteresis. The presence of a high density of lattice defects, dislocations, and nanoscale grain size significantly affects the martensitic transformation and phase change mechanisms. Also, any post-processing heat treatments, such as aging, can influence the SMAs' performance by raising the martensite transition temperature and generation of R, B, and α phase variants and other precipitates.

The application of any SPD technique is associated with the creation of high dislocation density, twining, shear bands, precipitation, and phase transformations; these can induce a stable, consistent, and improved superelastic response in the Nitinol alloy and other SMAs. But there is a critical grain size depending on the SMA; below this range, the shape memory properties may be lost. CGP processing of NiTi SMAs led to the generation of sharp grain boundaries, Ti_2Ni particles, and needle-like stress-induced martensite phases from primary austenite phases, possibly containing dislocations and twinning. The nanostructuring via CGP, in addition to enhancing mechanical properties, led to a favorable shape memory effect and proper superelastic response. The ECAP method has the capability of improving the SMAs' mechanical response, in which shear plastic straining is able to produce microstructures in the range of 100–250 nm in NiTi SMAs, along with enhancing the yield strength, tensile strength, maximum reaction stress, and recoverable strain. The ECAR method, in a similar way, can improve the mechanical properties of Cu-8.3Al–8Mn SMA and produce a combination of bainitic and martensitic structures. Also, the application of the HSHPT method on a Heusler shape memory alloy led to grain size reduction and a change in the ratio of different phases and their distribution, inducing a considerable drop in the martensitic transformation temperature, and affecting the magnetic and shape memory response. The HSHPT method can also produce plate-shaped-martensite needles, in the range of 50–120 nm, and many stacking faults in Fe–Mn–Si–Cr SMAs. As another SPD method, LLC processing of NiTi SMAs is accompanied by a martensitic reorientation, detwinning, and dynamic recrystallization that led to amorphization. This amorphization behavior was also observed in ARB-processed SMAs, in which extreme grain refinement, nanostructuring, and amorphization can lead to superior superelasticity response. Considering these results, SPD can be simultaneously used to improve

the mechanical properties and shape memory response of various shape memory alloys and its utilization may result in an extraordinarily high strength, ductility, and hardness, as well as low-temperature superplasticity.

Despite many studies having been conducted concerning shape memory alloys and their properties, still much research should be done to reach high-throughput SMAs with unique properties with advanced multifunctional applications. Therefore, in order to reach the next generation of advanced SMAs, many other investigations should be conducted to elucidate the exact effect of grain size and SPD utilization on the properties and performance of SMAs. In this regard, the texture and grain orientations should be carefully studied, and the microstructural evolutions with the related recrystallization mechanisms should be thoroughly considered, along with the post-processing treatments. Meanwhile, special attention should be given to the development and design of modern SMAs with composited, multilayered, and textured structures and multifunctional applications, by utilization of new SPD techniques. The modern ordered structures could be very interesting for future industrial requirements. It is hoped that this study will open the way for researchers in the field, and provide new ideas and approaches to those interested, in order to facilitate the process of obtaining these advanced shape memory alloys for the future.

Author Contributions: Conceptualization, M.E. and S.R.K.; methodology, S.A.; validation, M.E., S.A. and C.G.; formal analysis, M.S. and C.G.; investigation, S.A. and M.S.; resources, M.E., C.G. and Q.W.; data curation, M.E. and S.R.K.; writing—original draft preparation, S.A. and S.R.K.; writing—review and editing, M.E.; visualization, C.G. and Q.W.; supervision, M.E. and Q.W.; funding acquisition, Q.W. All authors have read and agreed to the published version of the manuscript.

Funding: This work was supported by the National Key Research and Development Program of China (Grant No. 2021YFB3701303) and the National Natural Science Foundation of China (No. U1902220).

Institutional Review Board Statement: Not applicable.

Informed Consent Statement: Not applicable.

Data Availability Statement: All data generated or analyzed during this study are included in this published article.

Conflicts of Interest: The authors declare no conflict of interest.

References

1. Ebrahimi, M.; Wang, Q.; Attarilar, S. A comprehensive review of magnesium-based alloys and composites processed by cyclic extrusion compression and the related techniques. *Prog. Mater. Sci.* **2023**, *131*, 101016. [CrossRef]
2. Langdon, T.G. Twenty-five years of ultrafine-grained materials: Achieving exceptional properties through grain refinement. *Acta Mater.* **2013**, *61*, 7035–7059. [CrossRef]
3. Edalati, K.; Horita, Z. A review on high-pressure torsion (HPT) from 1935 to 1988. *Mater. Sci. Eng. A* **2016**, *652*, 325–352. [CrossRef]
4. Valiev, R.Z.; Langdon, T.G. Principles of equal-channel angular pressing as a processing tool for grain refinement. *Prog. Mater. Sci.* **2006**, *51*, 881–981. [CrossRef]
5. Djavanroodi, F.; Omranpour, B.; Ebrahimi, M.; Sedighi, M. Designing of ECAP parameters based on strain distribution uniformity. *Prog. Nat. Sci. Mater. Int.* **2012**, *22*, 452–460. [CrossRef]
6. Attarilar, S.; Salehi, M.T.; Djavanroodi, F. Microhardness evolution of pure titanium deformed by equal channel angular extrusion. *Metall. Res. Technol.* **2019**, *116*, 1–10. [CrossRef]
7. Ebrahimi, M.; Djavanroodi, F.; Tiji, S.; Gholipour, H.; Gode, C. Experimental Investigation of the Equal Channel Forward Extrusion Process. *Metals* **2015**, *5*, 471–483. [CrossRef]
8. Wu, J.; Ebrahimi, M.; Attarilar, S.; Gode, C.; Zadshakoyan, M. Cyclic Extrusion Compression Process for Achieving Ultrafine-Grained 5052 Aluminum Alloy with Eminent Strength and Wear Resistance. *Metals* **2022**, *12*, 1627. [CrossRef]
9. Ebrahimi, M.; Wang, Q. Accumulative roll-bonding of aluminum alloys and composites: An overview of properties and performance. *J. Mater. Res. Technol.* **2022**, *19*, 4381–4403. [CrossRef]
10. Fan, R.; Attarilar, S.; Shamsborhan, M.; Ebrahimi, M.; Gode, C.; Özkavak, H.V. Enhancing mechanical properties and corrosion performance of AA6063 aluminum alloys through constrained groove pressing technique. *Trans. Nonferrous Met. Soc. China* **2020**, *30*, 1790–1802. [CrossRef]
11. Djavanroodi, F.; Ebrahimi, M.; Nayfeh, J.F. Tribological and mechanical investigation of multi-directional forged nickel. *Sci. Rep.* **2019**, *9*, 241. [CrossRef] [PubMed]

12. Ebrahimi, M.; Par, M.A. Twenty-year uninterrupted endeavor of friction stir processing by focusing on copper and its alloys. *J. Alloys Compd.* **2019**, *781*, 1074–1090. [CrossRef]
13. Ebrahimi, M.; Shamsborhan, M. Monotonic and dynamic mechanical properties of PTCAE aluminum. *J. Alloys Compd.* **2017**, *705*, 28–37. [CrossRef]
14. Ebrahimi, M. Fatigue Behaviors of Materials Processed by Planar Twist Extrusion. *Metall. Mater. Trans. A* **2017**, *48*, 6126–6134. [CrossRef]
15. Mohd, J.; Leary, M.; Subic, A.; Gibson, M.A. A review of shape memory alloy research, applications and opportunities. *Mater. Des.* **2014**, *56*, 1078–1113. [CrossRef]
16. Liang, L.; Xu, M.; Chen, Y.; Zhang, T.; Tong, W.; Liu, H.; Wang, H.; Li, H. Effect of welding thermal treatment on the microstructure and mechanical properties of nickel-based superalloy fabricated by selective laser melting. *Mater. Sci. Eng. A* **2021**, *819*, 141507. [CrossRef]
17. Miyazaki, S.; Otsuka, K. Development of Shape Memory Alloys. *ISIJ Int.* **1989**, *29*, 353–377. [CrossRef]
18. Ölander, A. An electrochemical investigation of solid cadmium-gold alloys. *J. Am. Chem. Soc.* **1932**, *54*, 3819–3833. [CrossRef]
19. Buehler, W.J.; Gilfrich, J.V.; Wiley, R.C. Effect of Low-Temperature Phase Changes on the Mechanical Properties of Alloys near Composition TiNi. *J. Appl. Phys.* **1963**, *34*, 1475. [CrossRef]
20. Furuya, Y.; Shimada, H. Shape memory actuators for robotic applications. *Mater. Des.* **1991**, *12*, 21–28. [CrossRef]
21. Babacan, N.; Atli, K.C.; Turkbas, O.S.; Karaman, I.; Kockar, B. The effect of dynamic aging on the cyclic stability of Cu73Al16Mn11 shape memory alloy. *Mater. Sci. Eng. A* **2017**, *701*, 352–358. [CrossRef]
22. Humbeeck, J. Van Non-medical applications of shape memory alloys. *Mater. Sci. Eng. A* **1999**, *273–275*, 134–148. [CrossRef]
23. Hartl, D.J.; Lagoudas, D.C. Aerospace applications of shape memory alloys. *Proc. Inst. Mech. Eng. Part G J. Aerosp. Eng.* **2007**, *221*, 535–552. [CrossRef]
24. Bil, C.; Massey, K.; Abdullah, E.J. Wing morphing control with shape memory alloy actuators. *J. Intell. Mater. Syst. Struct.* **2013**, *24*, 879–898. [CrossRef]
25. Jani, J.M.; Leary, M.; Subic, A. Shape memory alloys in automotive applications. *Appl. Mech. Mater.* **2014**, *663*, 248–253. [CrossRef]
26. Qi, Y.; Lapovok, R.; Estrin, Y. Microstructure and electrical conductivity of aluminium/steel bimetallic rods processed by severe plastic deformation. *J. Mater. Sci.* **2016**, *51*, 6860–6875. [CrossRef]
27. Zehetbauer, M.; Grössinger, R.; Krenn, H.; Krystian, M.; Pippan, R.; Rogl, P.; Waitz, T.; Würschum, R. Bulk nanostructured functional materials by severe plastic deformation. *Adv. Eng. Mater.* **2010**, *12*, 692–700. [CrossRef]
28. Guillem-Martí, J.; Herranz-Díez, C.; Shaffer, J.E.; Gil, F.J.; Manero, J.M. Mechanical and microstructural characterization of new nickel-free low modulus β-type titanium wires during thermomechanical treatments. *Mater. Sci. Eng. A* **2015**, *636*, 507–515. [CrossRef]
29. He, J.; Zhu, S.; Luo, C.; Niu, X.; Wang, Q. Size effect in fatigue modelling of defective materials: Application of the calibrated weakest-link theory. *Int. J. Fatigue* **2022**, *165*, 107213. [CrossRef]
30. Xu, H.; He, T.; Zhong, N.; Zhao, B.; Liu, Z. Transient thermomechanical analysis of micro cylindrical asperity sliding contact of SnSbCu alloy. *Tribol. Int.* **2022**, *167*, 107362. [CrossRef]
31. Sathish, S.; Mallik, U.S.; Raju, T.N. Microstructure and Shape Memory Effect of Cu-Zn-Ni Shape Memory Alloys. *J. Miner. Mater. Charact. Eng.* **2014**, *2*, 71–77. [CrossRef]
32. Liu, J.L.; Huang, H.Y.; Xie, J.X. Superelastic anisotropy characteristics of columnar-grained Cu-Al-Mn shape memory alloys and its potential applications. *Mater. Des.* **2015**, *85*, 211–220. [CrossRef]
33. Huang, W. On the selection of shape memory alloys for actuators. *Mater. Des.* **2002**, *23*, 11–19. [CrossRef]
34. Bhardwaj, A.; Gupta, A.K.; Padisala, S.K.; Poluri, K. Characterization of mechanical and microstructural properties of constrained groove pressed nitinol shape memory alloy for biomedical applications. *Mater. Sci. Eng. C* **2019**, *102*, 730–742. [CrossRef]
35. Sun, L.; Huang, W.M.; Ding, Z.; Zhao, Y.; Wang, C.C.; Purnawali, H.; Tang, C. Stimulus-responsive shape memory materials: A review. *Mater. Des.* **2012**, *33*, 577–640. [CrossRef]
36. Sakon, T.; Nagashio, H.; Sasaki, K.; Susuga, S.; Numakura, D.; Abe, M.; Endo, K.; Yamashita, S.; Nojiri, H.; Kanomata, T. Thermal strain and magnetization of the ferromagnetic shape memory alloy Ni52Mn25Ga23 in a magnetic field. *J. Phys. Chem. Solids* **2013**, *74*, 158–165. [CrossRef]
37. Li, Y.; Jiang, C.; Liang, T.; Ma, Y.; Xu, H. Martensitic transformation and magnetization of Ni–Fe–Ga ferromagnetic shape memory alloys. *Scr. Mater.* **2003**, *48*, 1255–1258. [CrossRef]
38. Namvari, M.; Laitinen, V.; Sozinov, A.; Saren, A.; Ullakko, K. Effects of 1 at.% additions of Co, Fe, Cu, and Cr on the properties of Ni-Mn-Ga-based magnetic shape memory alloys. *Scr. Mater.* **2023**, *224*, 115116. [CrossRef]
39. Dan, N.H.; Hau, K.X.; Yen, N.H.; Thi Thanh, P.; Ngoc, N.H.; Anh, T.V.; Nguyet Nga, N.T.; Anh, D.T.K. Structure and magnetic properties of Ni50−xCoxMn50−yAly (x = 5–9, y = 18–19) shape memory alloy ribbons. *J. Alloys Compd.* **2022**, *916*, 165470. [CrossRef]
40. Amako, Y.; Tanaka, S.; Nakashima, M.; Eto, T.; Adachi, Y.; Kanomata, T. 119Sn Mössbauer and magnetization studies of the Heusler alloy Ni2Mn1.48Sn0.52. *J. Phys. Chem. Solids* **2023**, *172*, 111101. [CrossRef]
41. Heczko, O.; Straka, L. Compositional dependence of structure, magnetization and magnetic anisotropy in Ni–Mn–Ga magnetic shape memory alloys. *J. Magn. Magn. Mater.* **2004**, *272–276*, 2045–2046. [CrossRef]

42. Wang, S.; Yang, R.; Lu, G.; Yi, L.; Liu, M.; Xu, Y.; Pan, L. Atomic occupation and role of Cr atoms in Cr-doped Ni43Co7Mn39Sn11 magnetic shape memory alloys. *J. Alloys Compd.* **2022**, *929*, 167315. [CrossRef]
43. Yang, H.; An, K.; Nie, Z.H.; Wang, Y.D.; Tang, B.; Peng, T. The anomalous staircase-like magnetization behavior and giant magnetocaloric effect in a Fe–Mn-Ga magnetic shape memory alloy. *Intermetallics* **2020**, *127*, 106975. [CrossRef]
44. Gao, W.; Yi, X.; Sun, B.; Fu, Y.; Meng, X. Low-cost (ZrCu)50-xTax high temperature shape memory alloys showing excellent shape memory effect. *Prog. Nat. Sci. Mater. Int.* **2022**, *32*, 369–374. [CrossRef]
45. Montecinos, S.; Cuniberti, A.; Sepúlveda, A. Grain size and pseudoelastic behaviour of a Cu–Al–Be alloy. *Mater. Charact.* **2008**, *59*, 117–123. [CrossRef]
46. Casciati, F.; Faravelli, L. Experimental characterisation of a Cu-based shape memory alloy toward its exploitation in passive control devices. *J. Phys. IV* **2004**, *115*, 299–306. [CrossRef]
47. Torra, V.; Isalgue, A.; Lovey, F.C.; Martorell, F.; Molina, F.J.; Sade, M.; Tachoire, H. Shape memory alloys: From the physical properties of metastable phase transitions to dampers for civil engineering applications. *J. Phys. IV* **2004**, *113*, 85–90. [CrossRef]
48. Figueroa, C.G.; Garcia-Castillo, F.N.; Jacobo, V.H.; Cortés-Pérez, J.; Schouwenaars, R. Microstructural and superficial modification in a Cu-Al-Be shape memory alloy due to superficial severe plastic deformation under sliding wear conditions. *IOP Conf. Ser. Mater. Sci. Eng.* **2017**, *194*, 012011. [CrossRef]
49. Zhang, Y.; He, X.; Xu, K.; Kang, Y.; Sun, H.; Liu, H.; Cao, Y.; Wei, S.; Li, Z.; Jing, C. Structural ordering, magnetic and electrical transport properties in Ni60-Fe13+Ga27 Heusler alloys. *J. Alloys Compd.* **2023**, *936*, 168242. [CrossRef]
50. Nikolaev, V.I.; Stepanov, S.I.; Yakushev, P.N.; Krymov, V.M.; Kustov, S.B. Burst-like shape recovery and caloric effects in Ni–Fe–Ga–Co single crystalline shape memory alloys. *Intermetallics* **2020**, *119*, 106709. [CrossRef]
51. Zhang, X.; Chen, H.; Li, S.; Niu, Y.; Yin, T.; Song, C.; Lang, R.; Cong, D.; Li, S.; Wang, Y.-D. Enhanced cyclability of superelasticity and elastocaloric effect in Cu and B co-doped Co-Ni-Ga shape memory alloys. *J. Alloys Compd.* **2022**, *918*, 165633. [CrossRef]
52. Mendonça, A.A.; Ghivelder, L.; Bernardo, P.L.; Cohen, L.F.; Gomes, A.M. Low hysteretic magnetostructural transformation in Cr-doped Ni-Mn-Ga Heusler alloy. *J. Alloys Compd.* **2023**, *938*, 168444. [CrossRef]
53. Tavares, S.; Yang, K.; Meyers, M.A. Heusler alloys: Past, properties, new alloys, and prospects. *Prog. Mater. Sci.* **2023**, *132*, 101017. [CrossRef]
54. Cao, P.; Tian, F.; Li, W.; Vitos, L.; Wang, Y. Ideal superelasticity in Ni-based Heusler alloys. *Acta Mater.* **2021**, *210*, 116816. [CrossRef]
55. Gurau, G.; Gurau, C.; Sampath, V.; Bujoreanu, L.G. Investigations of a nanostructured FeMnSi shape memory alloy produced via severe plastic deformation. *Int. J. Miner. Metall. Mater.* **2016**, *23*, 1315–1322. [CrossRef]
56. Jiang, S.; Hu, L.; Zhang, Y.; Liang, Y. Nanocrystallization and amorphization of NiTi shape memory alloy under severe plastic deformation based on local canning compression. *J. Non-Cryst. Solids* **2013**, *367*, 23–29. [CrossRef]
57. Sun, D.; Jiang, S.; Zhang, Y.; Yan, B.; Yu, J. Influence of annealing on incomplete detwinning and deformation twinning in equiatomic NiTi shape memory alloy undergoing severe plastic deformation. *J. Alloys Compd.* **2021**, *871*, 159550. [CrossRef]
58. Hu, L.; Jiang, S.; Zhang, Y.; Zhao, Y.; Liu, S.; Zhao, C. Intermetallics Multiple plastic deformation mechanisms of NiTi shape memory alloy based on local canning compression at various temperatures. *Intermetallics* **2016**, *70*, 45–52. [CrossRef]
59. Gunderov, D.V.; Kuranova, N.N.; Luk'Yanov, A.V.; Uksusnikov, A.N.; Prokof'Ev, E.A.; Yurchenko, L.I.; Valiev, R.Z.; Pushin, V.G. Application of severe plastic deformation by torsion to form amorphous and nanocrystalline states in large-size TiNi alloy sample. *Phys. Met. Metallogr.* **2009**, *108*, 131–138. [CrossRef]
60. Jiang, S.Y.; Zhao, Y.N.; Zhang, Y.Q.; Tang, M.; Li, C.F. Equal channel angular extrusion of NiTi shape memory alloy tube. *Trans. Nonferrous Met. Soc. China* **2013**, *23*, 2021–2028. [CrossRef]
61. Pushin, V.G.; Stolyarov, V.V.; Valiev, R.Z.; Lowe, T.C.; Zhu, Y.T. Nanostructured TiNi-based shape memory alloys processed by severe plastic deformation. *Mater. Sci. Eng. A* **2005**, *411*, 386–389. [CrossRef]
62. Zhang, X.; Xia, B.; Song, J.; Chen, B.; Tian, X.; Hao, Y.; Xie, C. Effects of equal channel angular extrusion and aging treatment on R phase transformation behaviors and Ti3Ni4 precipitates of Ni-rich TiNi alloys. *J. Alloys Compd.* **2011**, *509*, 6296–6301. [CrossRef]
63. Song, J.; Wang, L.M.; Zhang, X.N.; Sun, X.G.; Jiang, H.; Fan, Z.G.; Xie, C.Y.; Wu, M.H. Effects of second phases on mechanical properties and martensitic transformations of ECAPed TiNi and Ti-Mo based shape memory alloys. *Trans. Nonferrous Met. Soc. China* **2012**, *22*, 1839–1848. [CrossRef]
64. Fan, Z.G.; Xie, C.Y. Shape Memory Behavior of Ti-50.9at%Ni Alloy after ECAE Processes. *Mater. Sci. Forum* **2007**, *561–565*, 2313–2316. [CrossRef]
65. Zhang, X.; Song, J.; Huang, C.; Xia, B.; Chen, B.; Sun, X.; Xie, C. Microstructures evolution and phase transformation behaviors of Ni-rich TiNi shape memory alloys after equal channel angular extrusion. *J. Alloys Compd.* **2011**, *509*, 3006–3012. [CrossRef]
66. Zhang, X.; Song, J.; Jiang, H.; Sun, X.; Xie, C. Effects of ECAE and aging on phase transformations and superelasticity of a Ni-rich TiNi SMA. *Mater. Sci. Forum* **2011**, *682*, 185–191. [CrossRef]
67. Pushin, V.G.; Stolyarov, V.V.; Valiev, R.Z.; Kourov, N.I.; Kuranova, N.N.; Prokofiev, E.A.; Yurchenko, L.I. Features of structure and phase transformations in shape memory TiNi-based alloys after severe plastic deformation. *Ann. Chim. Sci. Matériaux* **2002**, *27*, 77–88. [CrossRef]
68. Arockiakumar, R.; Park, J.K. Effect of α-precipitation on the superelastic behavior of Ti-40 wt.%Nb-0.3 wt.%O alloy processed by equal channel angular extrusion. *Mater. Sci. Eng. A* **2010**, *527*, 2709–2713. [CrossRef]

69. Zhang, P.; Ma, A.; Lu, S.; Lin, P.; Jiang, J.; Ma, H.; Chu, C. Effect of equal channel angular pressing and heat treatment on the microstructure of Cu-Al-Be-B shape memory alloy. *Mater. Lett.* **2009**, *63*, 2676–2679. [CrossRef]
70. Alizadeh, M.; Avazzadeh, M. Evaluation of Cu-26Zn-5Al shape memory alloy fabricated by accumulative roll bonding process. *Mater. Sci. Eng. A* **2019**, *757*, 88–94. [CrossRef]
71. Alizadeh, M.; Dashtestaninejad, M.K. Fabrication of manganese-aluminum bronze as a shape memory alloy by accumulative roll bonding process. *Mater. Des.* **2016**, *111*, 263–270. [CrossRef]
72. Ostovari Moghaddam, A.; Mazinani, A.; Ketabchi, M. Effect of Accumulative Roll Bonding and Equal Channel Angular Rolling on Microstructural and Mechanical Properties of Cu–Al–Mn Shape Memory Alloys. *Trans. Indian Inst. Met.* **2017**, *70*, 1901–1909. [CrossRef]
73. Gurau, G.; Gurau, C.; Tolea, F.; Valeanu, M.; Sampath, V.; Bujoreanu, L.G. Effect of Severe Plastic Deformation on the Structure and Magnetic Behaviour of an Fe-Mn-Si Shape Memory Alloy. *Adv. Mater. Res.* **2017**, *1143*, 240–246. [CrossRef]
74. Popescu, B.; Gurau, C.; Gurau, G.; Tolea, M.; Sofronie, M.; Tolea, F. Martensitic Transformation and Magnetic Properties of Ni57Fe18Ga25 Shape Memory Alloy Subjected to Severe Plastic Deformation. *Trans. Indian Inst. Met.* **2021**, *74*, 2491–2498. [CrossRef]
75. Gurau, C.; Gurau, G.; Tolea, F.; Sampath, V. Structural evolution of the niti/nifega smart hybrid material during severe plastic deformation. *Dig. J. Nanomater. Biostructures* **2019**, *14*, 539–546.
76. Waitz, T.; Antretter, T.; Fischer, F.D.; Karnthaler, H.P. Size effects on martensitic phase transformations in nanocrystalline NiTi shape memory alloys. *Mater. Sci. Technol.* **2008**, *24*, 934–940. [CrossRef]
77. Sun, Q.P.; He, Y.J. A multiscale continuum model of the grain-size dependence of the stress hysteresis in shape memory alloy polycrystals. *Int. J. Solids Struct.* **2008**, *45*, 3868–3896. [CrossRef]
78. Meng, Q.; Rong, Y.; Hsu, T.Y. Nucleation barrier for phase transformations in nanosized crystals. *Phys. Rev. B* **2002**, *65*, 174118. [CrossRef]
79. Meng, Q.; Zhou, N.; Rong, Y.; Chen, S.; Hsu (Xu Zuyao), T.Y.; Zuyao, X. Size effect on the Fe nanocrystalline phase transformation. *Acta Mater.* **2002**, *50*, 4563–4570. [CrossRef]
80. Lee, T.-J.; Kim, W.-J. Effect of Severe Plastic Deformation and Post-Deformation Heat Treatment on the Microstructure and Superelastic Properties of Ti-50.8 at.% Ni Alloy. *Materials* **2022**, *15*, 7822. [CrossRef]
81. Satheesh Kumar, S.S.; Raghu, T. Structural and mechanical behaviour of severe plastically deformed high purity aluminium sheets processed by constrained groove pressing technique. *Mater. Des.* **2013**, *57*, 114–120. [CrossRef]
82. Ebrahimi, M.; Attarilar, S.; Djavanroodi, F.; Gode, C.; Kim, H.S. Wear properties of brass samples subjected to constrained groove pressing process. *Mater. Des.* **2014**, *63*, 531–537. [CrossRef]
83. Garudapalli, A.; Bhardwaj, A.; Oswal, K.; Mathur, D.; Gupta, A.K. Microstructural, Mechanical, and Superelastic Behavior of Thermo-Mechanically Processed Nitinol Alloy. *Shape Mem. Superelasticity* **2021**, *7*, 503–514. [CrossRef]
84. Rohatgi, A.; Vecchio, K.S.; Gray, G.T. The influence of stacking fault energy on the mechanical behavior of Cu and Cu-Al alloys: Deformation twinning, work hardening, and dynamic recovery. *Metall. Mater. Trans. A* **2001**, *32*, 135–145. [CrossRef]
85. Vercammen, S.; Blanpain, B.; De Cooman, B.C.; Wollants, P. Cold rolling behaviour of an austenitic Fe–30Mn–3Al–3Si TWIP-steel: The importance of deformation twinning. *Acta Mater.* **2004**, *52*, 2005–2012. [CrossRef]
86. Xiao, G.H.; Tao, N.R.; Lu, K. Effects of strain, strain rate and temperature on deformation twinning in a Cu–Zn alloy. *Scr. Mater.* **2008**, *59*, 975–978. [CrossRef]
87. Attarilar, S.; Djavanroodi, F.; Ebrahimi, M.; Al-Fadhalah, K.J.; Wang, L.; Mozafari, M. Hierarchical Microstructure Tailoring of Pure Titanium for Enhancing Cellular Response at Tissue-Implant Interface. *J. Biomed. Nanotechnol.* **2021**, *17*, 115–130. [CrossRef]
88. Duerig, T.W.; Melton, K.N.; Stöckel, D. *Engineering Aspects of Shape Memory Alloys*; Butterworth-Heinemann: Oxford, UK, 2013.
89. Shaeri, M.H.; Shaeri, M.; Ebrahimi, M.; Salehi, M.T.; Seyyedein, S.H. Effect of ECAP temperature on microstructure and mechanical properties of Al-Zn-Mg-Cu alloy. *Prog. Nat. Sci. Mater. Int.* **2016**, *26*, 182–191. [CrossRef]
90. Ebrahimi, M.; Shaeri, M.H.; Gode, C.; Armoon, H.; Shamsborhan, M. The synergistic effect of dilute alloying and nanostructuring of copper on the improvement of mechanical and tribological response. *Compos. Part B Eng.* **2019**, *164*, 508–516. [CrossRef]
91. Lin, Z.; Wang, L. The Ultrafine-Grained Titanium and Biomedical Titanium Alloys Processed by Severe Plastic Deformation (SPD). *SOJ Mater. Sci. Eng.* **2013**, *1*, 1. [CrossRef]
92. Djavanroodi, F.; Ebrahimi, M.; Rajabifar, B.; Akramizadeh, S. Fatigue design factors for ECAPed materials. *Mater. Sci. Eng. A* **2010**, *528*, 745–750. [CrossRef]
93. Sutou, Y.; Omori, T.; Yamauchi, K.; Ono, N.; Kainuma, R.; Ishida, K. Effect of grain size and texture on pseudoelasticity in Cu-Al-Mn-based shape memory wire. *Acta Mater.* **2005**, *53*, 4121–4133. [CrossRef]
94. Hsu, C.A.; Wang, W.H.; Hsu, Y.F.; Rehbach, W.P. The refinement treatment of martensite in Cu-11.38 wt.%Al-0.43 wt.%Be shape memory alloys. *J. Alloys Compd.* **2009**, *474*, 455–462. [CrossRef]
95. Sergueeva, A.V.; Song, C.; Valiev, R.Z.; Mukherjee, A.K. Structure and properties of amorphous and nanocrystalline NiTi prepared by severe plastic deformation and annealing. *Mater. Sci. Eng. A* **2003**, *339*, 159–165. [CrossRef]
96. Gurău, G.; Gurău, C.; Potecaşu, O.; Alexandru, P.; Bujoreanu, L.-G. Novel High-Speed High Pressure Torsion Technology for Obtaining Fe-Mn-Si-Cr Shape Memory Alloy Active Elements. *J. Mater. Eng. Perform.* **2014**, *23*, 2396–2402. [CrossRef]
97. Gurau, G.; Gurau, C.; Tolea, F.; Sampath, V. Structural Change in Ni-Fe-Ga Magnetic Shape Memory Alloys after Severe Plastic Deformation. *Materials* **2019**, *12*, 1939. [CrossRef]

98. Panigrahi, A.; Sulkowski, B.; Waitz, T.; Ozaltin, K.; Chrominski, W.; Pukenas, A.; Horky, J.; Lewandowska, M.; Skrotzki, W.; Zehetbauer, M. Mechanical properties, structural and texture evolution of biocompatible Ti–45Nb alloy processed by severe plastic deformation. *J. Mech. Behav. Biomed. Mater.* **2016**, *62*, 93–105. [CrossRef]
99. An, X.H.; Lin, Q.Y.; Sha, G.; Huang, M.X.; Ringer, S.P.; Zhu, Y.T.; Liao, X.Z. Microstructural evolution and phase transformation in twinning-induced plasticity steel induced by high-pressure torsion. *Acta Mater.* **2016**, *109*, 300–313. [CrossRef]
100. Sun, D.; Jiang, S.; Xing, X.; Yan, B.; Yu, J.; Zhang, Y. Microstructures and Mechanical Properties of Equiatomic NiTi Shape Memory Alloy Undergoing Local Canning Compression and Subsequent Annealing. *Met. Mater. Int.* **2021**, *27*, 4901–4910. [CrossRef]
101. Zhang, Y.; Jiang, S.; Hu, L. Investigation of Dynamic Recrystallization of NiTi Shape Memory Alloy Subjected to Local Canning Compression. *Metals* **2017**, *7*, 208. [CrossRef]
102. Nishida, M.; Ii, S.; Kitamura, K.; Furukawa, T.; Chiba, A.; Hara, T.; Hiraga, K. New deformation twinning mode of B19′ martensite in Ti-Ni shape memory alloy. *Scr. Mater.* **1998**, *39*, 1749–1754. [CrossRef]
103. Hua, P.; Wang, B.; Yu, C.; Han, Y.; Sun, Q. Shear-induced amorphization in nanocrystalline NiTi micropillars under large plastic deformation. *Acta Mater.* **2022**, *241*, 118358. [CrossRef]
104. Ko, W.-S.; Choi, W.S.; Xu, G.; Choi, P.-P.; Ikeda, Y.; Grabowski, B. Dissecting functional degradation in NiTi shape memory alloys containing amorphous regions via atomistic simulations. *Acta Mater.* **2021**, *202*, 331–349. [CrossRef]
105. Zhang, Y.; Jiang, S.; Wang, M. Atomistic investigation on superelasticity of NiTi shape memory alloy with complex microstructures based on molecular dynamics simulation. *Int. J. Plast.* **2020**, *125*, 27–51. [CrossRef]
106. Ko, W.-S.; Jeon, J.B. Atomistic simulations on orientation dependent martensitic transformation during nanoindentation of NiTi shape-memory alloys. *Comput. Mater. Sci.* **2021**, *187*, 110127. [CrossRef]
107. Tsuji, N.; Saito, Y.; Utsunomiya, H.; Tanigawa, S. Ultra-fine grained bulk steel produced by accumulative roll-bonding (ARB) process. *Scr. Mater.* **1999**, *40*, 795–800. [CrossRef]
108. Lim, Y.G.; Han, S.H.; Choi, E.; Kim, W.J. Shape memory and superelasticity of nanograined Ti-51.2 at.% Ni alloy processed by severe plastic deformation via high-ratio differential speed rolling. *Mater. Charact.* **2018**, *145*, 284–293. [CrossRef]
109. Kahani Khabushan, J.; Bazzaz Bonabi, S. Investigating of the Microstructure and Mechanical Properties of Al-Based Composite Reinforced with Nano-Trioxide Tungsten via Accumulative Roll Bonding Process. *Open J. Met.* **2017**, *07*, 9–23. [CrossRef]